



UNIVERSITÀ
DI TRENTO

DEPARTMENT OF PHYSICS

Master degree in Physics

**Chaotic dynamics of an electronic
implementation of the
Burridge-Knopoff model**

Graduant:

Manuel BITTO

Supervisor:

Leonardo RICCI

Co-supervisor:

Alessio PERINELLI

24 October 2024

Contents

Introduction	v
1 An electronic analog of the Burridge-Knopoff model	1
1.1 Mechanical Burridge-Knopoff model	1
1.1.1 Motion of two coupled blocks	2
1.1.2 Dimensionless system	3
1.2 Electronic analog for the motion of two blocks	3
1.3 Characterization of the single block behavior	5
1.3.1 Breadboard implementation	5
1.3.2 Integrated board implementation	6
1.4 Characterization of the double block behavior	7
2 Chaos in theory and experiments	9
2.1 Dynamical systems	9
2.2 Formal definition of chaos	10
2.3 The issue of detecting chaos	10
2.4 The embedding procedure	11
2.5 Correlation dimension	13
2.6 Maximum Lyapunov exponent	14
2.7 A method for detecting chaos	15
2.7.1 The embedding lattice	15
3 Chaos analysis of multiple coupled blocks	17
3.1 Chaos plots	18
3.2 Conclusions	54
3.3 Attractor plots	55
Bibliography	62

Introduction

Chapter 1

An electronic analog of the Burridge-Knopoff model

1.1 Mechanical Burridge-Knopoff model

The Burridge-Knopoff (BK) spring-block model [1] is a two-dimensional system of massive blocks lying on a rough horizontal surface. Each block is connected to its nearest neighbors by a set of springs, and linked through another spring to an upper horizontal ceiling moving with constant velocity with respect to the lower plate, as shown in Fig. 1.1.

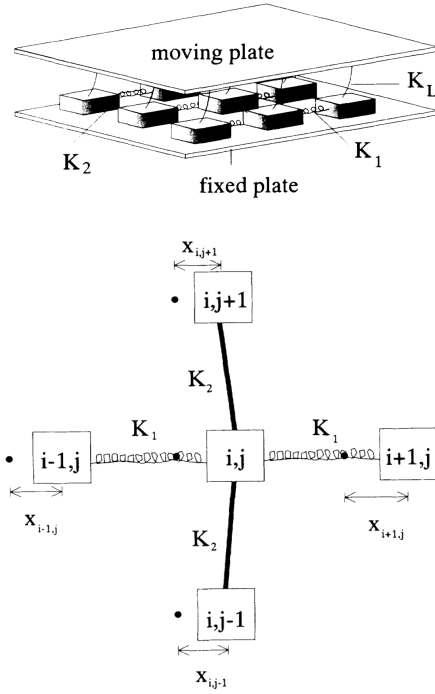


Figure 1.1: Visual representation of the Burridge-Knopoff spring-block model. K_1 and K_2 are the elastic constants, respectively, of the horizontal and vertical springs, while K_L is the elastic constant of the springs connecting the blocks and the moving plate. The figure below represents the interaction between a block and its four nearest neighbors, as a function of the displacement $x_{i,j}$. Figure adapted from Ref. [2].

The blocks are driven by the relative movement of the two rigid plates. When the force on one block reaches some threshold value F_{th} , the block slips, and it is reasonable to assume that the force on that block becomes zero. Then, the force on the four nearest neighbors is increased, often resulting in further slips, and an avalanche can occur.

The purpose of the BK model is the description of the dynamical behavior of real faults, whereby a constant, slow driving motion of plates produces an accumulation of “stress” up to a threshold at which such stress is released through an abrupt motion – i.e., an earthquake – of one or more of the system’s constituent parts.

1.1.1 Motion of two coupled blocks

The mechanical BK model for the motion of two coupled blocks is shown schematically in Fig. 1.2. The upper ceiling moves with respect to the surface with a constant velocity u_d . Let x_1, x_2 be the displacements of the block positions relative to a state in which the springs are relaxed, and u_1, u_2 the velocities of the blocks in the lower surface frame, so that $u_i = u_d + \dot{x}_i$ with $i = 1, 2$.

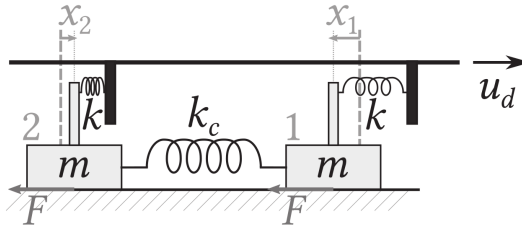


Figure 1.2: Two-blocks mechanical BK model. The upper ceiling, which the blocks are coupled to via springs with elastic constant k , is dragged with constant velocity u_d with respect to the underlying surface. This surface exerts a nonlinear, velocity-dependent friction F to each block’s motion. Figure adapted from Ref. [3].

The equations of motion are thus given by

$$\begin{aligned} m \frac{du_1}{dt} &= -kx_1 - k_c(x_1 - x_2) - F(u_1), \\ \frac{dx_1}{dt} &= u_1 - u_d, \\ m \frac{du_2}{dt} &= -kx_2 - k_c(x_2 - x_1) - F(u_2), \\ \frac{dx_2}{dt} &= u_2 - u_d, \end{aligned} \tag{1.1}$$

where m is the mass of the blocks, k is the elastic constant of the springs that connect the blocks to the ceiling, k_c is the elastic constant of the spring linking the two blocks, and $F(u)$ is the nonlinear velocity-dependent friction. The velocities are assumed to be non-negative.

1.1.2 Dimensionless system

It is possible to render this system dimensionless by defining the following dimensionless quantities (i takes the values 1 and 2): a time $\tau \equiv t\sqrt{k/m}$, a velocity $\nu_i \equiv u_i/u_0$, a position $\xi_i \equiv x_i\sqrt{k/m}/u_0$, a friction $\varphi(\nu_i) \equiv F(\nu_i)/(u_0\sqrt{mk})$ and a parameter $\lambda \equiv k_c/k$. The four equations of motion can then be written as

$$\begin{aligned}\frac{d\nu_i}{d\tau} &= -(1 + \lambda)\xi_i + \lambda\xi_{3-i} - \varphi(\nu_i), \\ \frac{d\xi_i}{d\tau} &= \nu_i - \nu_d.\end{aligned}\tag{1.2}$$

There exists a relative freedom in the choice of the friction $\varphi(\nu)$, provided that (i) $\varphi(\nu < 0) = 0$, (ii) $\varphi(\nu \geq 0) \geq 0$ and (iii) $\varphi(\nu)$ decreases down to zero from a maximum value $\varphi(0)$ that occurs at $\nu = 0$.

It is useful to define the equations of motion also in the case of a lower surface moving with a positive dimensionless velocity $\Delta\nu$, so that $\nu'_i = \nu_i + \Delta\nu$ and $\nu'_d = \nu_d + \Delta\nu$. The system of equations becomes:

$$\begin{aligned}\frac{d\nu'_i}{d\tau} &= -(1 + \lambda)\xi_i + \lambda\xi_{3-i} - \varphi(\nu'_i - \Delta\nu), \\ \frac{d\xi_i}{d\tau} &= \nu'_i - \nu'_d.\end{aligned}\tag{1.3}$$

1.2 Electronic analog for the motion of two blocks

In order to analyze the properties of the BK model, it is possible to build an electronic circuit which differential equations are the same as Eqs. 1.3. The first implementation was done by Field, Venturi and Nori [4] by drawing a direct parallelism between mechanical and electrical quantities. The idea was to use capacitance as mass, inductance as the reciprocal of elastic constant, voltage as velocity and current as position. However, this implementation has two main drawbacks. The first one is the usage of inductances, which are typically bulky and have intrinsically large tolerances compared with other components, resulting in higher uncertainties; moreover, their tunability is very low. The second issue is that the current is a state variable, and it is less straightforward to measure it with respect to voltage.

It is possible to use another implementation [3] which does not rely on inductances and uses only voltages as state variables. In order to do so it is necessary to rewrite the system equations as integral equations, so that they can be implemented by electronic integrators that are more stable than the differentiators. The new state variables are defined as $V_i \equiv \nu_i V_0$ and $W_i \equiv \xi_i V_0$ and the new time constant is given by $\tau = RC$, where R and C are suitably chosen resistance and capacitance. Integrating the system of Eqs. 1.3 for a moving surface and replacing $V'_i \equiv V_i + \Delta V$ and $V'_d \equiv V_d + \Delta V$, where $V_d \equiv V_0\nu_d$ and $\Delta V \equiv V_0\Delta\nu$, leads to the following system of equations:

$$V_i + \Delta V = -\frac{1}{RC} \int \left[(1 + \lambda)W_i - \lambda W_{3-i} + V_0 \varphi \left(\frac{V_i}{V_0} \right) \right] dt, \quad (1.4)$$

$$W_i = -\frac{1}{RC} \int (V_d - V_i) dt,$$

where $\lambda = R/R_c$ and R_c is a suitably chosen resistance.

These differential equations are implemented by the circuit shown in Fig. 1.3, which makes use of resistors, capacitors, diodes and operational amplifiers, without any inductance. Assuming for a while that ΔV and the nonlinear element $\varphi(V_i/V_0)$ were not present, the two integrations above could be promptly implemented by considering the black part of the circuit diagram.

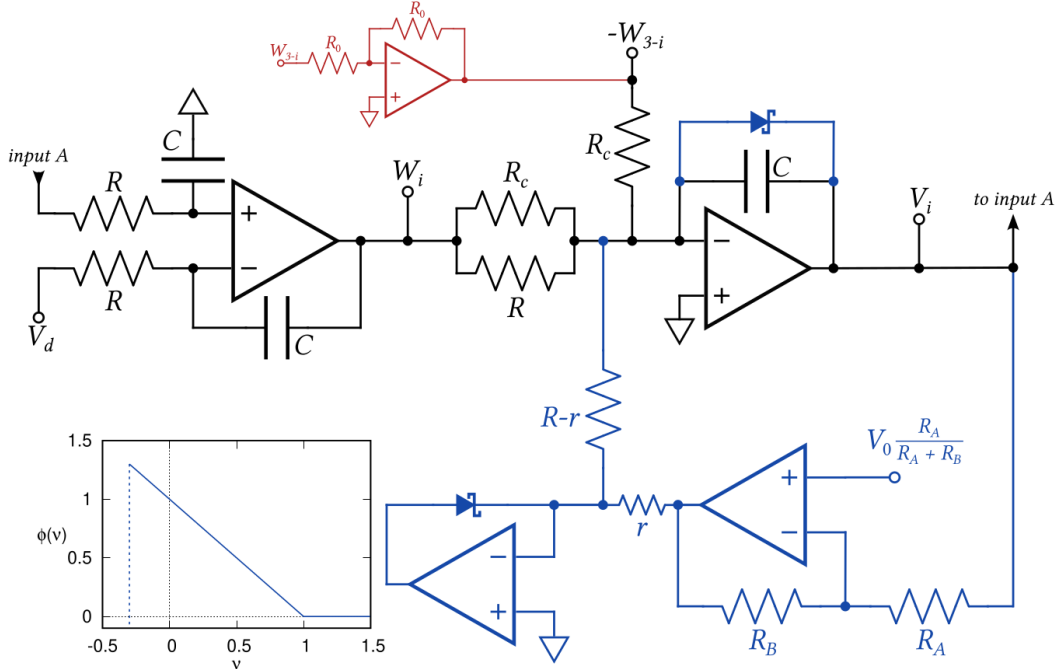


Figure 1.3: Inductorless representation of the BK model. The circuit diagram refers to a single block, labeled by $i = 1, 2$. The bottom left plot shows the characteristic of the nonlinear element, i.e. the blue part of the diagram. The red part is a standard inverting operational amplifier, which is necessary for the coupling between two blocks. Figure adapted from Ref. [3].

The nonlinear term is instead represented by the blue part of the diagram and it is implemented as follows. A Schottky diode is inserted on the feedback network on the integrator producing V_i ; this ensures that V_i does not drop below $-V_{\text{diode}}$, where $V_{\text{diode}} \approx 0.3$ V. In order to not contradict the constraint that the “velocity” must be always non-negative, it is necessary to set $\Delta V = V_{\text{diode}}$. In this way the first of the constraints set in Sec. 1.1.2, i.e. $\varphi(V_i < 0) = 0$ is satisfied, since the voltage cannot drop below zero.

The nonlinear friction element consists in a linear drop for the analog of the velocity-weakening force, and it is implemented using two additional op-amps as

follows. The output of the first op-amp is given by $V_0 - V_i R_B / R_A$. Downstream of the resistor r , this voltage is prevented to drop below zero by an active clamp made of the second op-amp which has a diode in its feedback network. The resulting voltage is fed back into the integrator generating V_i through an additional resistor $R - r$.

1.3 Characterization of the single block behavior

With the aim of analyzing the circuit represented in Fig. 1.3, it is necessary to characterize its behavior. The first characterization concerns the function of a single block, in the absence of couplings. In this case $\lambda = 0$ and the differential equations of the system can be simplified as (the subscript i is omitted):

$$\begin{aligned} \frac{d^2V}{dt^2} + \frac{1}{\tau} \varphi' \left(\frac{V}{V_0} \right) \frac{dV}{dt} + \frac{1}{\tau^2} (V - V_d) &= 0, \\ \frac{dW}{dt} &= \frac{1}{\tau} (V - V_d). \end{aligned} \tag{1.5}$$

where φ' is the derivative of the friction with respect to the velocity V . The equation for the velocity is of the kind met in the classical description of stick-slip vibrations [5], i.e. of the self-sustained oscillations induced by friction. This means that an oscillating behavior for V and W has to be expected.

In order to check the validity of these equations, the circuit was physically implemented in two different manners. The first implementation was done on a breadboard using large electronic components; the main issue with this system is that it is not scalable, due to the fact that a single circuit occupies half of the entire space on the breadboard. The second one consists instead in an integrated board in which 25 circuits like the one in Fig. 1.3 were implemented; the scalability issue is solved in this case, so that this board could be utilized to study the behavior of many coupled blocks, as will be done in the next chapters.

1.3.1 Breadboard implementation

The breadboard implementation was made using 1N5817 Schottky diodes and OP27 op-amps; these op-amps were supplied with $V_{CC} = \pm 12$ V. The nominal values for the resistances and capacitors are $R = R_c = 10$ k Ω , $R_A = R_B = 10$ k Ω , $r = 1.8$ k Ω and $C = 100$ nF, so that the characteristic time of the circuit is $\tau = 1$ ms. The input voltages are $V_0 = 1$ V and the variable voltage V_d , while the output voltages are V and W (the subscript i is omitted).

The single block behavior of this circuit is shown in Fig. 1.4. As expected by Eqs. 1.5, both the velocity V and the position W exhibit an oscillating behavior. While W closely resembles a sinusoidal wave, V possesses a lower clamping that makes it different from a simple wave; this clamping is due to the presence of the Schottky diodes, which prevent that the velocity becomes negative, as discussed in Sec. 1.2. In the end, both the frequency and the amplitude of the waves depend on the driving voltage V_d .

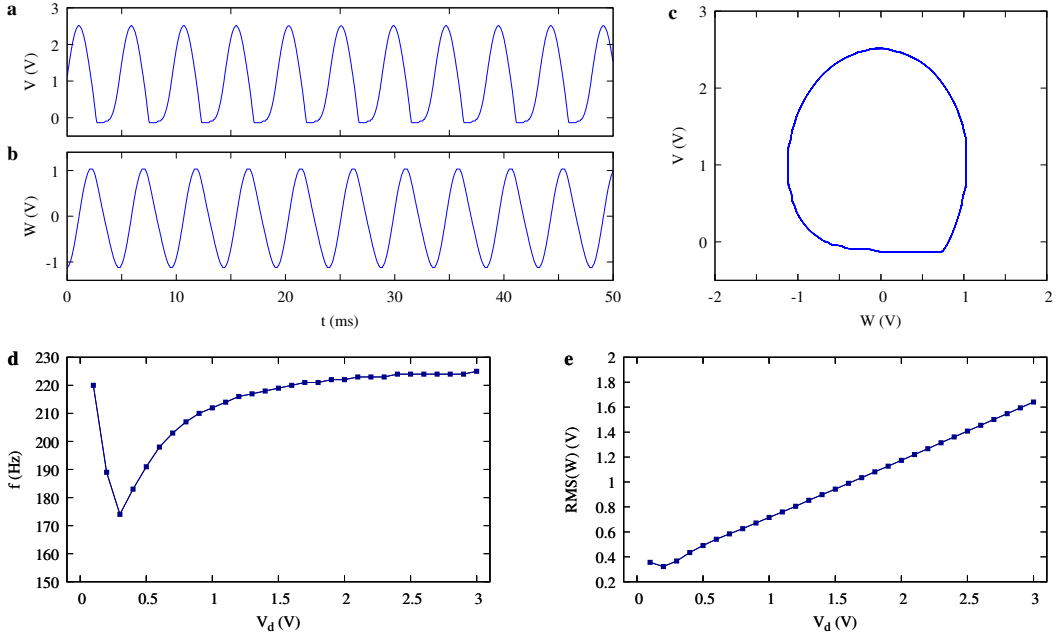


Figure 1.4: Oscillating behavior for the circuit implemented on the breadboard. (a) Plot of W and (b) of V as a function of time, for $V_d = 1$ V. (c) Phase portrait (Lissajous figure) of V versus W . (d) Frequency and (e) root mean square amplitude of the output signal W as a function of the parameter V_d .

1.3.2 Integrated board implementation

The circuit diagram for each of the 25 chips on the integrated board is equivalent to the one shown in Fig. 1.3. The only differences with the breadboard implementation concern the nonlinear components, i.e. the use of DFLS1100 Schottky diodes and quad operational amplifiers OP470, which should offer comparable performances to the components used in the previous section, i.e. 1N5817 Schottky diodes and OP27 op-amps.

A comparison between the single block behavior of this circuit and the one implemented in the previous section is shown in Fig. 1.5. The most notable difference is the amplitude of the waveforms and of the Lissajous figures, which is higher in the integrated board case. Another discrepancy between the two plots lies in the frequency behavior at low driving voltage V_d , i.e. the initial “drop” in the frequency is more pronounced in the breadboard case with respect to the integrated circuit. These distinctions are all probably due to the different diodes and op-amps utilized in the two cases, but they do not modify the actual dynamics of the circuit.

Despite being slightly different, both implementations comply with the oscillating behavior predicted by Eqs. 1.5. It is thus reasonable to assume that both the integrated circuit and the one on the breadboard can potentially be a consistent physical implementation of the BK model. In order to furtherly strengthen this hypothesis, an analysis on the behavior of two coupled blocks will be carried out in the next section. From now on, only the integrated board implementation will be considered, due to the scalability issues that were discussed beforehand.

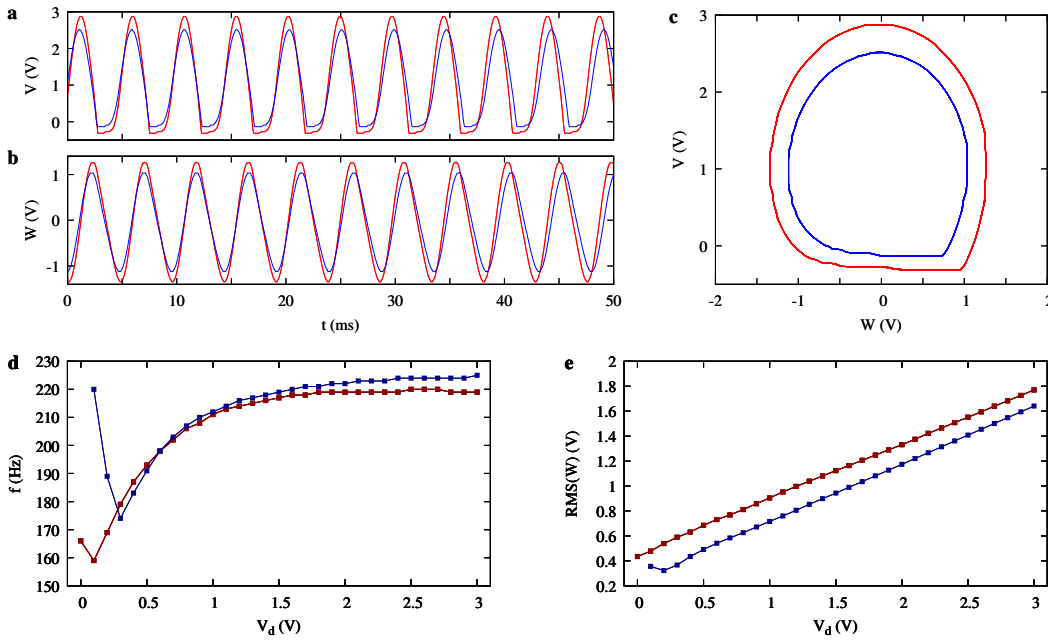


Figure 1.5: Oscillating behavior for the circuit implemented on the integrated board (red) and the one implemented on the breadboard (blue). (a) Plot of W and (b) of V as a function of time, for $V_d = 1$ V. (c) Phase portrait (Lissajous figure) of V versus W . (d) Frequency and (e) root mean square amplitude of the output signal W as a function of the parameter V_d .

1.4 Characterization of the double block behavior

The coupling between two blocks is performed by connecting the inverted voltage $-W_2$ of the second block to the inverting input of the op-amp generating V_1 on the first block (see Fig. 1.3), and viceversa, in order to comply with Eqs. 1.4.

The behavior of the two coupled blocks is shown in Fig. 1.6. By looking at the waveforms $V_i(t)$ and $W_i(t)$ it is possible to notice that the simple periodic behavior is no longer observed. Furthermore, the Lissajous figures do not show a stationary orbit like the single block case. This hints that the dynamics in the presence of coupling might be chaotic, i.e. deterministic but unpredictable, and surely non-periodic.

Another way to check the presence of chaos in the system is to make use of a bifurcation diagram, i.e. the distribution of the local maxima of a state variable (position, velocity) as a function of an external parameter (driving force). This diagram is shown in Fig. 1.7 for the position W_1 (W_2 behaves similarly) as a function of V_d . The scan of the V_d parameter was carried out by switching off the circuit's power supply, changing the voltage V_d , and the switching the power supply back on. This ensured that the recorded evolution was independent of the previous state. It is possible to notice that the dynamics is richer for $V_d \lesssim 0.1$ V, where several maxima can be detected. In contrast, for $V_d \gtrsim 0.1$ V, only one maximum can be observed; in this regime the system behaves similarly to the single block case, manifesting periodic sinusoidal-like oscillations.

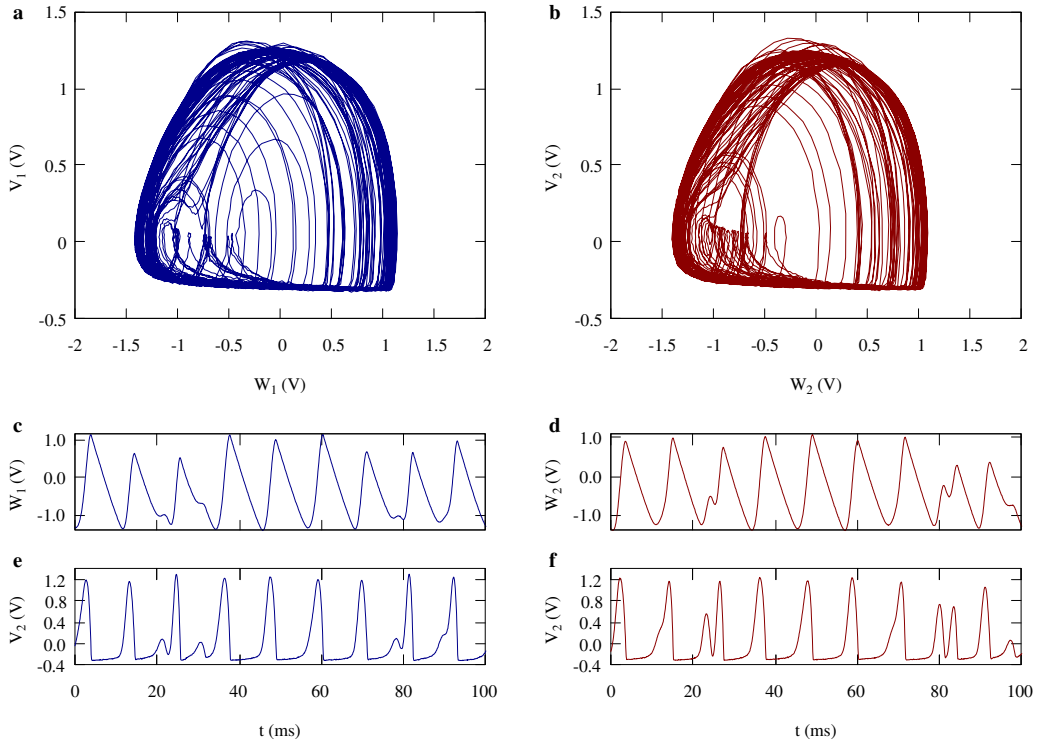


Figure 1.6: Chaotic behavior of two coupled blocks for $V_d = 0.05$ V. Phase portraits of V_i vs W_i for the first (a) and second (b) block, for a total time of 1 s. Time series plots for W_1 (c), V_1 (e), W_2 (d) and V_2 (f), for a total time of 100 ms.

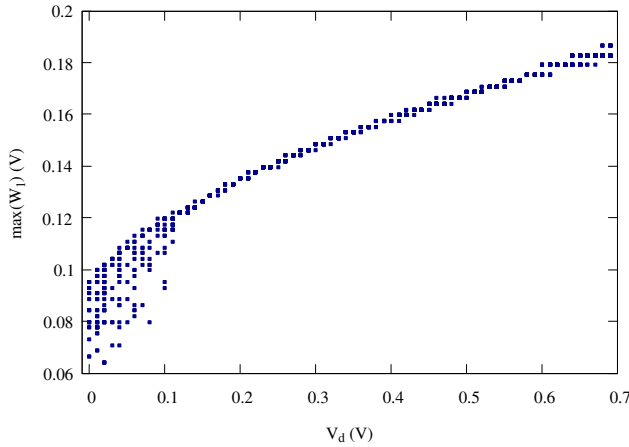


Figure 1.7: Bifurcation diagram for two coupled blocks. The local maxima of W_1 are plotted as a function of the external parameter V_d , which is varied in steps of 10 mV.

It is therefore safe to assume that, for low driving voltages V_d , the coupled system of two blocks shows a chaotic behavior. The reason why this does not occur at higher voltages might be that the driving force is so strong that the blocks behave independently of it. Nonetheless, these analyses are not enough to say that this circuit is actually a chaotic system. In order to prove this statement, it is necessary to define the mathematical conditions that characterize a chaotic system.

Chapter 2

Chaos in theory and experiments

2.1 Dynamical systems

The concept of dynamical systems is quite general, since anything that moves can be considered as a dynamical system [6]. If these changes are driven by specific rules, we say that the system is deterministic; otherwise, if the rules are random, it is stochastic. The main feature of chaotic systems is the fact that they are unpredictable despite being deterministic; in order to better explain the meaning of this statement, it is essential to involve some mathematical definitions.

The instantaneous state of a dynamical system is described by a vector \mathbf{s} within a state space \mathcal{S} (typically, $\mathcal{S} \subseteq \mathbb{R}^M$). The state vector evolves in time according to an evolution operator \mathcal{E}_t such that:

$$\mathbf{s}(t + t_0) = \mathcal{E}_t[\mathbf{s}(t_0)]. \quad (2.1)$$

In theoretical systems the state space \mathcal{S} is well-defined and the evolution operator \mathcal{E}_t is given; in most cases, \mathcal{E}_t is defined by a set of differential equations which can be solved, analytically or numerically, to find the system's evolution $\mathbf{s}(t)$ out of the initial conditions $\mathbf{s}(0)$.

A dynamical system is defined to be linear if the superposition principle holds, i.e.:

$$\mathcal{E}_t[c_1\mathbf{s}_1 + c_2\mathbf{s}_2] = c_1\mathcal{E}_t[\mathbf{s}_1] + c_2\mathcal{E}_t[\mathbf{s}_2]. \quad (2.2)$$

If the last equality is not satisfied the system is said to be nonlinear. Nonlinearity is a necessary (but not sufficient) condition for the system to be chaotic.

In experimentally observed systems the state space is not always fully accessible; moreover, the evolution operator \mathcal{E}_t is rarely known. Observing a system consists in recording some signal $y(t)$ out of it through some measurement function \mathcal{M} acting on the system's state, i.e. $y(t) = \mathcal{M}[\mathbf{s}(t)]$. This continuous signal is always sampled and digitized, producing a finite time series (or sequence) $\{y_n\}$ with $n = 1, \dots, \ell$.

2.2 Formal definition of chaos

An universally accepted mathematical definition of chaos does not exists but a commonly used definition is the following, originally formulated by Robert L. Devaney [7].

Three conditions are necessary and sufficient to define a system as chaotic: (i) sensitivity to initial conditions; (ii) topological transitivity; (iii) density of periodic orbits.

Going into detail:

- (i) Sensitivity to initial conditions is a property that characterizes chaotic systems and makes their evolution hard to predict.

Given two initial conditions $\mathbf{s}_1(0)$, $\mathbf{s}_2(0)$ that are arbitrarily close within the state space ($\|\mathbf{s}_1(0) - \mathbf{s}_2(0)\| < \varepsilon$), the system having sensitive dependence on initial conditions means that the two trajectories evolving out of these initial conditions diverge exponentially in time, i.e. for large t :

$$\|\mathbf{s}_1(t) - \mathbf{s}_2(t)\| \propto e^{\lambda t}, \quad (2.3)$$

where λ is called maximum Lyapunov exponent (MLE). In order for the system to be chaotic, λ has to be positive.

It is also important that the orbits $\mathbf{s}_1(t)$, $\mathbf{s}_2(t)$ remain bounded at large t , otherwise, if orbits went to infinity, it would be simple for their distance to diverge exponentially.

The most important consequence of this property is that, as far as we are able to precisely measure the initial state of a system, there will always be a small error (given for example by measuring instruments) which can grow rapidly over time. Therefore, even if we know exactly the deterministic laws governing time evolution, our predictions on the behaviour of the system after a certain time will no longer be reliable. Furthermore, if the precision with which we measure the state of the system in the initial instant is improved by a factor of 10, we only gain a $\log(10)$ factor for the maximum time for which the predictions are accurate.

- (ii) Topological transitivity is the property according to which a chaotic trajectory eventually connects any region of the state space with any other. In other words, the state space of a chaotic system cannot be decomposed into disjoint subsets.
- (iii) Density of periodic orbits means that for any given point in the state space there is a periodic orbit that passes arbitrarily close to it, i.e. periodic orbits make up a dense set.

2.3 The issue of detecting chaos

When dealing with experimentally observed systems, the precise laws that describe the dynamics are unknown. What is known is the time series, which can be used

to assess condition (i) of Devaney's definition of chaos. Instead, conditions (ii) and (iii) are difficult to identify with the time series only. However, there are observable consequences. In particular, the time evolution of a chaotic system in the state space always converges to an object called strange attractor, characterized by a fractal structure [6, 8]. This means that strange attractors exhibit self-similarity (or self-affinity¹) and have a non-integer dimensionality.

To understand what it means to have non-integer dimensionality, suppose to consider a fractal object with dimension $1 < D < 2$. We know in general that if we have an object of dimension D (assuming that it has a mass density), taking an arbitrary point in it and considering an open ball centered in that point, we can measure the mass contained in the ball as a function of the radius. For small distances $m(r) \propto r^D$. For the same density and radius, the fractal "weighs" more than a line but less than a surface, as if a dense set (which is the set of the periodic points) had been removed from the surface.

Self-similarity, instead, is the exhibition of similar patterns at increasingly smaller scales; in other words, a fractal does not appear simplified when we see it zoomed. Despite strange attractors also existing in non-chaotic systems [10], the estimate of the system's non-integer dimension is often used as a tool to identify chaos.

Another important property allows us to identify chaos: the trajectory winds around forever never repeating on a strange attractor and the time series arising by chaotic systems are aperiodic and characterized by broad, noise-like Fourier spectra [11]. This also means that linear techniques such as fast Fourier transform (FFT) applied to sequences cannot distinguish between a chaotic system and a stochastic one, e.g. a Gaussian white noise source (GWN).

One more necessary requirement to sustain a chaotic flow is that the number of independent dimensions has to be at least three, assuming no discontinuities [12]; this is due to the fact that with two or less independent variables the trajectory will eventually intersect itself, which cannot happen due to the aperiodic nature of chaotic dynamics.

2.4 The embedding procedure

In experimentally observed systems it is only possible to utilize the finite time series $\{y_n\}$, with the aim to at least obtain some invariant quantities, e.g. the maximum Lyapunov exponent or the "effective" dimension of the system. Under certain conditions, a procedure exists with which it is possible to reconstruct the entire state space using only one variable, which is a function of the state space vector $\mathbf{s}(t)$. This procedure is called "time delay embedding" [13].

Embedding consists in building a sequence of m -dimensional vectors \mathbf{Y}_n by picking

¹In general, it is more correct to speak of self-affinity, since in the case of self-similarity the object is scaled by the same amount in all space directions, but in self-affinity scaling is not necessarily identical in all directions [9].

m time-delayed samples of the sequence y_n , i.e.:

$$\mathbf{Y}_n = (y_n, y_{n+L}, y_{n+2L}, \dots, y_{n+(m-1)L}), \quad (2.4)$$

where the parameter L is an integer number and is called “lag”. It is perfectly equivalent to make use of a “causal” version of Eq. 2.4 in which the chosen samples are y_{n-kL} instead of y_{n+kL} , with $k = 0, \dots, m - 1$ [14].

It has been proven by Takens [15] and Mañé [16] that if the parameters m (dimension) and L (lag) are suitably chosen, the reconstructed state space evolution is topologically identical to the actual state space dynamics. This means that a “good” embedding provides a smooth one-to-one map from the original state space evolution to the reconstructed one, therefore enabling us to estimate the properties of the original system that are invariant under this mapping.

The two conditions under which Takens’ theorem holds regard the embedding parameters (m, L) . The first one requires that $m > 2D$, where D is the dimension of the manifold corresponding to the time evolution of the system, which is not known a priori; this condition can be relaxed to $m > D$ if estimating correlation dimension [17]. The second one states that L is not a multiple of the period of any system’s orbit [18].

Aside from these two minimal conditions, since Takens’ theorem is an existence theorem, it does not give any hint on how to find the best embedding parameters. The reason for this is that as long as the two conditions are met, every choice for the couple (m, L) is good for reconstruct the dynamics; however, this is valid only for noiseless, finely sampled and infinitely long sequences. In reality, the issue of optimal embedding is a very active field in the physics of chaos, and several techniques have been developed in order to overcome this problem [19, 20, 21].

Considering the dimension m , choosing $m \gg 1$ ensures, in principle, that m is greater than $2D$. However, if m is too large the directions orthogonal to the deterministic noiseless trajectory will be dominated by noise and will not provide extra information; in other words, supposing that m_0 is the minimum dimension for which the system is correctly embedded, the remaining $m - m_0$ dimensions would be populated by noise, being thus redundant and resulting in an increase of the computational cost. Moreover, the larger is the embedding dimension m , the fewer independent embedding vectors are available, which is an issue considering the finiteness of the time series.

The choice on the lag L is also not trivial. If L is too short, the elements of the embedding vectors \mathbf{Y}_n will be strongly correlated, resulting in all the points being clustered on the diagonal of the reconstructed space; in presence of noise, therefore, the trajectory would be indistinguishable from the diagonal itself. On the other hand, a too large L presents the opposite problem, i.e. the elements of \mathbf{Y}_n to be completely uncorrelated with each other; this implies that the time evolution is “blurred”, in the sense that the trajectory is folded over on itself and the system evolution is lost.

2.5 Correlation dimension

Before addressing the issue of optimal embedding, it is important to formally define the invariant quantities that will be used to decide if an experimentally observed system is chaotic or not, the first one being the correlation dimension [11].

The simplest definition of dimension is the (integer) number of coordinates that are needed to specify a state, e.g. the number of differential equations of a system. This is the geometrically related to the concept of how (hyper) volumes scale as a function of a characteristic length parameter. One way to estimate the dimension of a set of points is the box-counting method, which consists in partitioning the space in hypercubes of size l and by counting, as a function of l , the fraction $\eta(l)$ of these hypercubes containing at least one point of the set. The dimension can then be calculated using the fact that $\eta(l \rightarrow 0) \propto l^D$. Since this method is very sensitive and computationally demanding [22], it is useful to search for other ways to estimate the dimension.

Given a set of points $\{\mathbf{Y}_n\}$ within an m -dimensional space partitioned in hypercubes of size l , and given p_i the fraction of points of the set that fall within the i -th hypercube, the generalized dimension is defined as [6]:

$$D_q = \lim_{l \rightarrow 0} \frac{1}{q-1} \frac{\log(\sum_i p_i^q)}{\log l}. \quad (2.5)$$

This definition provides a whole spectrum of invariant quantities for $-\infty < q < \infty$. For example, D_0 is exactly the dimension calculated with the box-counting method, i.e.:

$$D_0 = \lim_{l \rightarrow 0} \frac{\log(\sum_i 1)}{\log l} = \lim_{l \rightarrow 0} \frac{\log \eta(l)}{\log l}. \quad (2.6)$$

The dimension for $q \rightarrow 1$ can instead be calculated using L'Hospital's rule, resulting in:

$$D_1 = \lim_{l \rightarrow 0} \frac{\sum_i p_i \log p_i}{\log l}. \quad (2.7)$$

D_1 is called informational dimension [11] due to the numerator being related to information entropy. In a uniform fractal, in which $p_i = 1/N$ for every i , $D_1 = D_0$; instead, if the p_i are different $D_1 < D_0$. This is true in general for every q , namely $D_i \leq D_j$ if $i > j$, when the equality only holds in a uniform fractal.

Finally, one of the most utilized dimensions in chaos theory is the correlation dimension, defined as:

$$D_2 = \lim_{l \rightarrow 0} \frac{\log(\sum_i p_i^2)}{\log l}. \quad (2.8)$$

The numerator constitutes a two-point correlation function, measuring the probability of finding a pair of random points within a given partition element, just as the numerator in the definition of D_1 measures the probability of finding one point in a given element.

The reason why correlation dimension is so utilized lies in the fact that there is a very efficient way to estimate it, observed by Grassberger and Procaccia [23]. Due to the exponential divergence of the trajectories, most pairs $(\mathbf{Y}_i, \mathbf{Y}_j)$ with $i \neq j$ will be

dynamically uncorrelated pairs of essentially random points. The points lie however on the attractor, therefore they will be spatially correlated. This spatial correlation can be measured with the correlation integral $C(r)$, defined as:

$$C(r) = \lim_{\ell \rightarrow \infty} \frac{1}{\ell^2} \times \{\text{number of pairs } (i, j) \text{ whose distance is less than } r\}, \quad (2.9)$$

where ℓ is the total number of points in the reconstructed space. Grassberger and Procaccia proved that for small distances the correlation integral grows as $C(r) \propto r^{D_2}$. It is thus possible to estimate the correlation dimension by extracting random pairs of vectors in the embedded sequence, evaluating then a “sample” version of Eq. 2.9, namely:

$$C_{m,L}(r) = \frac{1}{N_{\text{pairs}}} \sum_{i,j} \theta(r - \|\mathbf{Y}_i - \mathbf{Y}_j\|), \quad (2.10)$$

where $\theta(x)$ is the Heaviside function and the subscript m,L indicates the dependence of this sample correlation integral on the embedding parameters.

A source of error regarding the estimation of $C(r)$ are temporal correlations within the input sequence, which can lead to underestimates of the dimension D_2 [24] or spurious contributions even in the case of stochastic sequences [25]. This issue can be avoided by selecting pairs of points that are distant in time more than some delay c_0 , i.e. constraining $|i - j| \geq c_0$. Typically, c_0 is chosen to be the first zero of the autocorrelation function [24] or its first minimum [26].

2.6 Maximum Lyapunov exponent

The second fundamental invariant quantity that characterizes a chaotic system is the maximum Lyapunov exponent (MLE) [11]. There are as many Lyapunov exponents as the number of state space dimensions: each exponent λ_i corresponds to one of the independent directions along which fiducial volumes within the state space contract ($\lambda_i < 0$) or expand ($\lambda_i > 0$) in an infinitesimal time interval. The MLE λ_1 is the most relevant of the spectrum, since its sign establishes whether the system stabilizes on a fixed point ($\lambda_1 < 0$), stabilizes on a limit cycle ($\lambda_1 = 0$) or is unstable ($\lambda_1 > 0$). A positive MLE is the main hallmark of chaos.

It is possible to estimate the MLE through the embedded sequence by making use of the so-called divergence rate method [27]. This method is based on the evaluation of the time-dependent divergence exponent $\Lambda(k)$, which quantifies the average separation of nearby trajectories. The estimation of this exponent is done by selecting random pairs (i, j) of neighboring vectors in the embedded sequence $\{\mathbf{Y}_n\}$, i.e. such that $\|\mathbf{Y}_i - \mathbf{Y}_j\| < r$, where r is some “shell radius”; the divergence exponent is then calculated as:

$$\Lambda_{m,L}(k) = \frac{1}{N_{\text{pairs}}} \sum_{i,j} \log \left(\frac{\|\mathbf{Y}_{i+k} - \mathbf{Y}_{j+k}\|}{\|\mathbf{Y}_i - \mathbf{Y}_j\|} \right), \quad (2.11)$$

where the subscript m,L indicates once again the dependence on the embedding parameters.

The time-dependent divergence exponent measures the progressive separation, as a function of the time delay k , of the trajectories corresponding to initially close points $\mathbf{Y}_i, \mathbf{Y}_j$. The initial proximity of the vector pairs is tuned by changing the shell radius r , which is typically estimated as the distance corresponding to the a given percentile p of the sample distribution of all Euclidean distances [28, 29].

Like in Section 2.5, it is important that the time separation between the pairs (i, j) is greater than the autocorrelation time, i.e. $|i - j| \geq c_0$ [24, 26].

If the underlying system is chaotic, $\Lambda(k)$ is expected to grow linearly with k , as a result of the exponentially increasing numerator within the logarithm of Eq. 2.11. Suitably fitting this linear growth provides the value of the MLE. The growth of $\Lambda(k)$ cannot continue for arbitrarily large values of k : eventually, the separation becomes comparable to the size of the attractor and the divergence exponent saturates.

2.7 A method for detecting chaos

The most utilized tools for detecting chaos, namely the embedding procedure, the correlation dimension and the maximum Lyapunov exponent, have now been introduced. It is now possible to establish an efficient procedure which not only searches for the best embedding parameters (m, L) , but also provides estimates for the invariant quantities that characterize chaos [20].

2.7.1 The embedding lattice

The scalar sequence $\{y_n\}$ is obtained by sampling the signal $y(t)$ with a sampling time T ; the time series is then supposed to be standardized as $y \rightarrow (y - \bar{y})/\bar{\sigma}$, where \bar{y} and $\bar{\sigma}$ are the sequence's sample mean and sample standard deviation, respectively.

Since a single optimal (m, L) does not necessarily exist, the embedding of the sequence is carried out for several values of the embedding parameters, considering that a set of (m, L) can provide reconstructions of the underlying dynamics that are equivalently good. More specifically, the procedure is carried out for each element of an embedding lattice, i.e. $\{(m, L) | m \in [2, m_{\max}], L \in [1, L_{\max}]\}$.

Suitable embedding choices are expected to comply with two requirements concerning the corresponding embedding window $w = (m - 1)L T$, which corresponds to the time span covered by each embedding vector. On the one hand, the embedding window has to be larger than the redundancy time τ_R , so that the points in the reconstructed space are not too close to the diagonal, as discussed in Section 2.4. On the other hand, the embedding window has to be smaller than the irrelevance time τ_I , after which the points are causally disconnected and the noise overcomes the dynamics.

The above requirements can then be expressed as $\tau_R/T \lesssim w \lesssim \tau_I/T$. In the embedding lattice, each window w identifies a hyperbola. Therefore, the irrelevance and redundancy times correspond to two hyperbolae within the embedding lattice, and the region bounded by them is where suitable embedding choices can be expected.

2.7.2 The divergence exponent

The next step of the procedure consists in calculating the maximum Lyapunov exponent and the correlation dimension. An efficient manner to do this is making use of the divergence exponent $\Lambda(k)$. As was already discussed in Section 2.6, if $\Lambda(k)$ exhibits a linear behavior it is possible to estimate the MLE as the slope of the curve.

For sufficiently large values of k , the divergence exponent $\Lambda(k)$ reaches a saturation value Λ_{pl} , referred to as a “plateau”. In the case of a chaotic source of finite correlation dimension ν , the plateau turns out to linearly depend on the logarithm of the percentile p [20]:

$$\Lambda_{\text{pl}} = \Lambda' - \frac{1}{\nu} \log p, \quad (2.12)$$

where Λ' is a constant that depends on the embedding parameters.

Chapter 3

Chaos analysis of multiple coupled blocks

3.1 Chaos plots

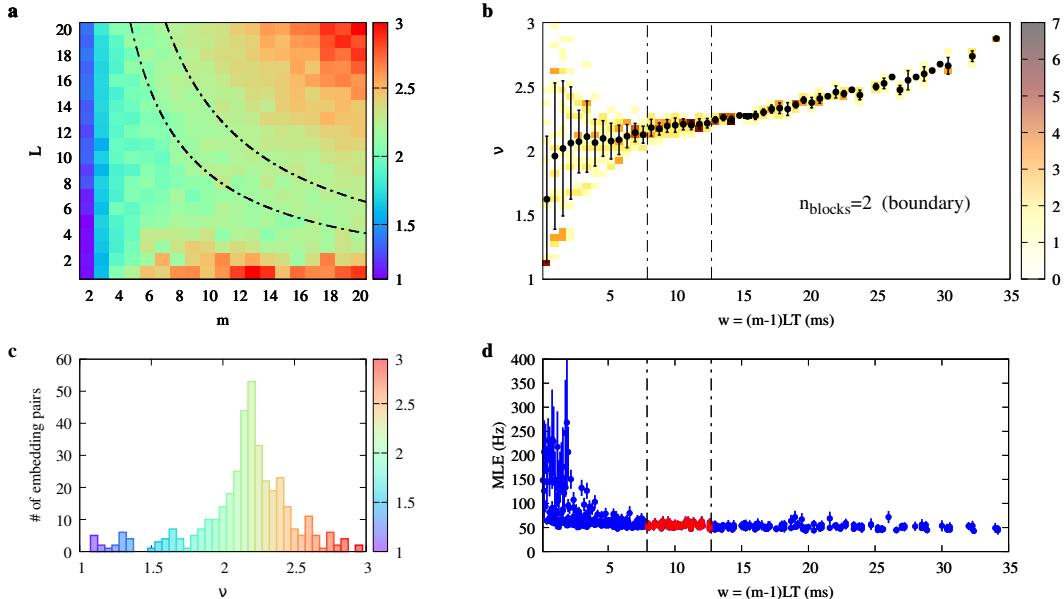


Figure 3.1: “Chasing chaos” analysis of the experimental W_1 time series obtained by setting $V_d = 0.05$ V with 2 coupled blocks. (a) Map of estimated correlation dimension ν vs. embedding pair (m, L) . The black, dash-dotted hyperbolae bound the region of uniform ν corresponding to the interval of the embedding window w highlighted in (b) and (d). (b) Sample joint distribution of (w, ν) for the ν -map in (a). Black dots and the related errorbars correspond to the expected value and the related uncertainty of ν for each given value (bin) of w . A uniformity region, highlighted by the dash-dotted vertical lines, is identified. (c) Histogram of the estimated ν . (d) Distribution of MLE as a function of w . Each point and the related uncertainty corresponds to the value assessed on an embedding pair by using the divergence rate method. A cluster of points, marked in red, can be identified in the uniformity region of (b), also highlighted here.

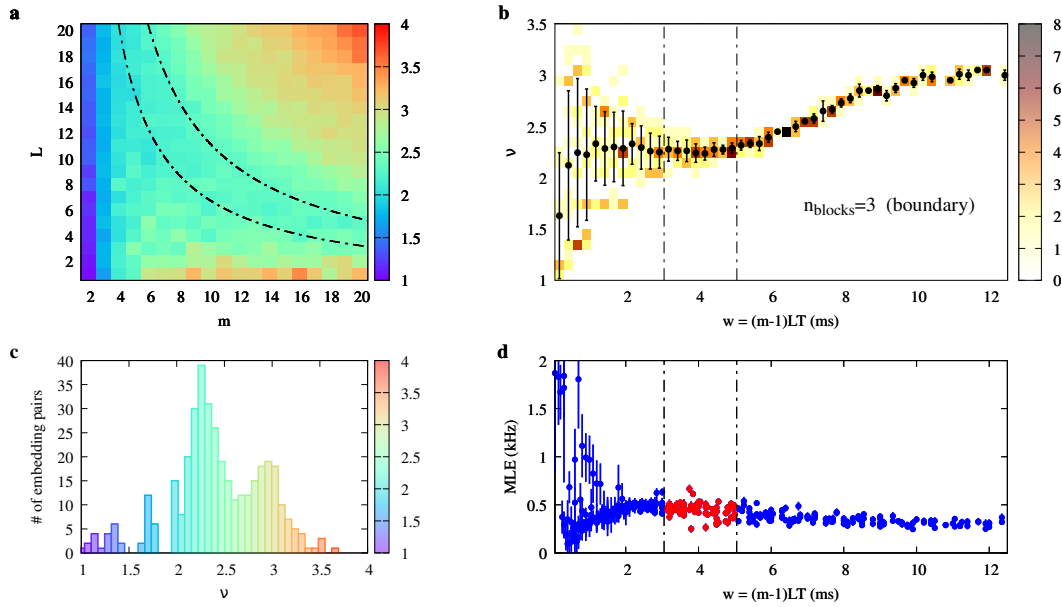


Figure 3.2: “Chasing chaos” analysis of the experimental W_1 time series obtained by setting $V_d = 0.05$ V with 3 coupled blocks. (a) Map of estimated correlation dimension ν vs. embedding pair (m, L) . The black, dash-dotted hyperbolae bound the region of uniform ν corresponding to the interval of the embedding window w highlighted in (b) and (d). (b) Sample joint distribution of (w, ν) for the ν -map in (a). Black dots and the related errorbars correspond to the expected value and the related uncertainty of ν for each given value (bin) of w . A uniformity region, highlighted by the dash-dotted vertical lines, is identified. (c) Histogram of the estimated ν . (d) Distribution of MLE as a function of w . Each point and the related uncertainty corresponds to the value assessed on an embedding pair by using the divergence rate method. A cluster of points, marked in red, can be identified in the uniformity region of (b), also highlighted here.

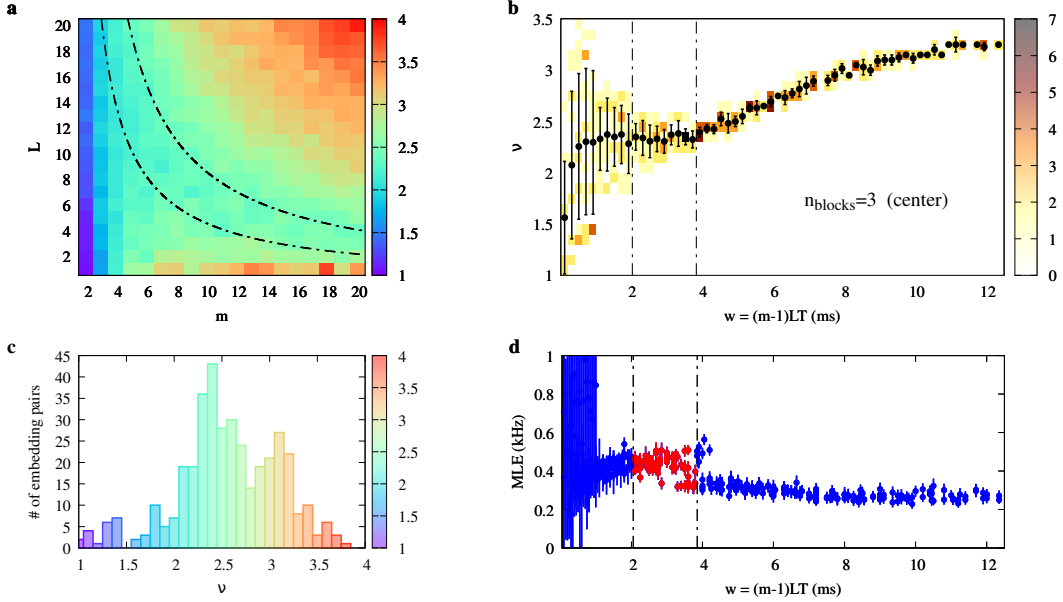


Figure 3.3: “Chasing chaos” analysis of the experimental W_2 time series obtained by setting $V_d = 0.05$ V with 3 coupled blocks. (a) Map of estimated correlation dimension ν vs. embedding pair (m, L) . The black, dash-dotted hyperbolae bound the region of uniform ν corresponding to the interval of the embedding window w highlighted in (b) and (d). (b) Sample joint distribution of (w, ν) for the ν -map in (a). Black dots and the related errorbars correspond to the expected value and the related uncertainty of ν for each given value (bin) of w . A uniformity region, highlighted by the dash-dotted vertical lines, is identified. (c) Histogram of the estimated ν . (d) Distribution of MLE as a function of w . Each point and the related uncertainty corresponds to the value assessed on an embedding pair by using the divergence rate method. A cluster of points, marked in red, can be identified in the uniformity region of (b), also highlighted here.

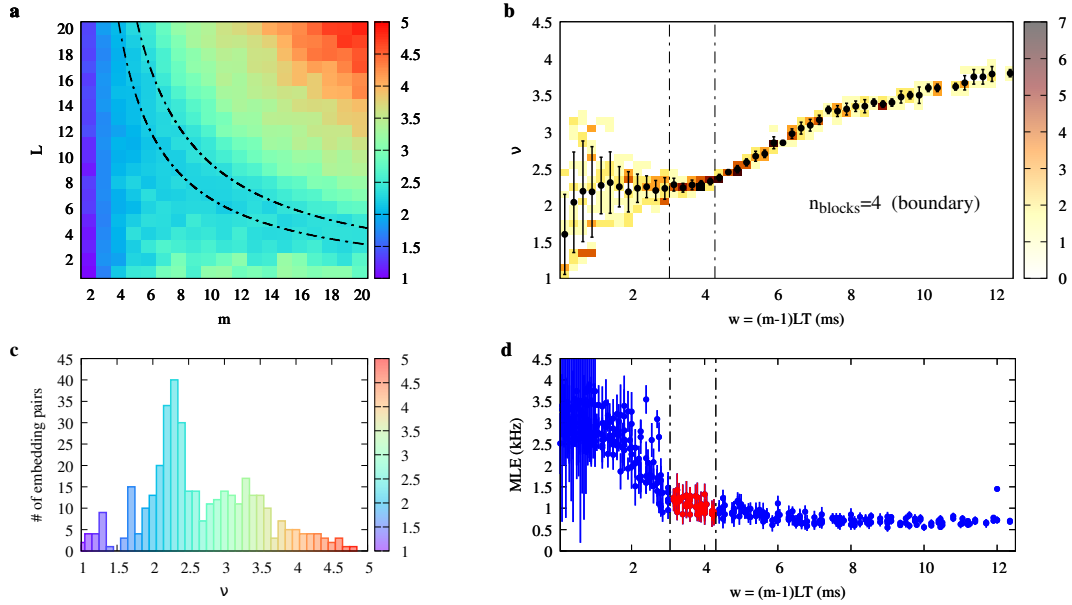


Figure 3.4: “Chasing chaos” analysis of the experimental W_1 time series obtained by setting $V_d = 0.05$ V with 4 coupled blocks. (a) Map of estimated correlation dimension ν vs. embedding pair (m, L) . The black, dash-dotted hyperbolae bound the region of uniform ν corresponding to the interval of the embedding window w highlighted in (b) and (d). (b) Sample joint distribution of (w, ν) for the ν -map in (a). Black dots and the related errorbars correspond to the expected value and the related uncertainty of ν for each given value (bin) of w . A uniformity region, highlighted by the dash-dotted vertical lines, is identified. (c) Histogram of the estimated ν . (d) Distribution of MLE as a function of w . Each point and the related uncertainty corresponds to the value assessed on an embedding pair by using the divergence rate method. A cluster of points, marked in red, can be identified in the uniformity region of (b), also highlighted here.

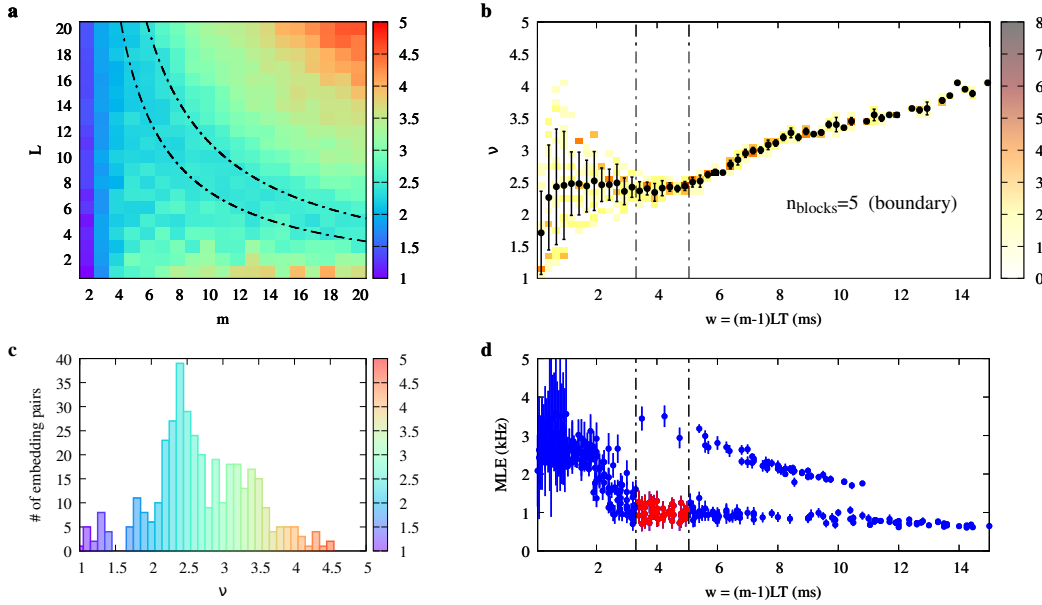


Figure 3.5: “Chasing chaos” analysis of the experimental W_1 time series obtained by setting $V_d = 0.05$ V with 5 coupled blocks. (a) Map of estimated correlation dimension ν vs. embedding pair (m, L) . The black, dash-dotted hyperbolae bound the region of uniform ν corresponding to the interval of the embedding window w highlighted in (b) and (d). (b) Sample joint distribution of (w, ν) for the ν -map in (a). Black dots and the related errorbars correspond to the expected value and the related uncertainty of ν for each given value (bin) of w . A uniformity region, highlighted by the dash-dotted vertical lines, is identified. (c) Histogram of the estimated ν . (d) Distribution of MLE as a function of w . Each point and the related uncertainty corresponds to the value assessed on an embedding pair by using the divergence rate method. A cluster of points, marked in red, can be identified in the uniformity region of (b), also highlighted here.

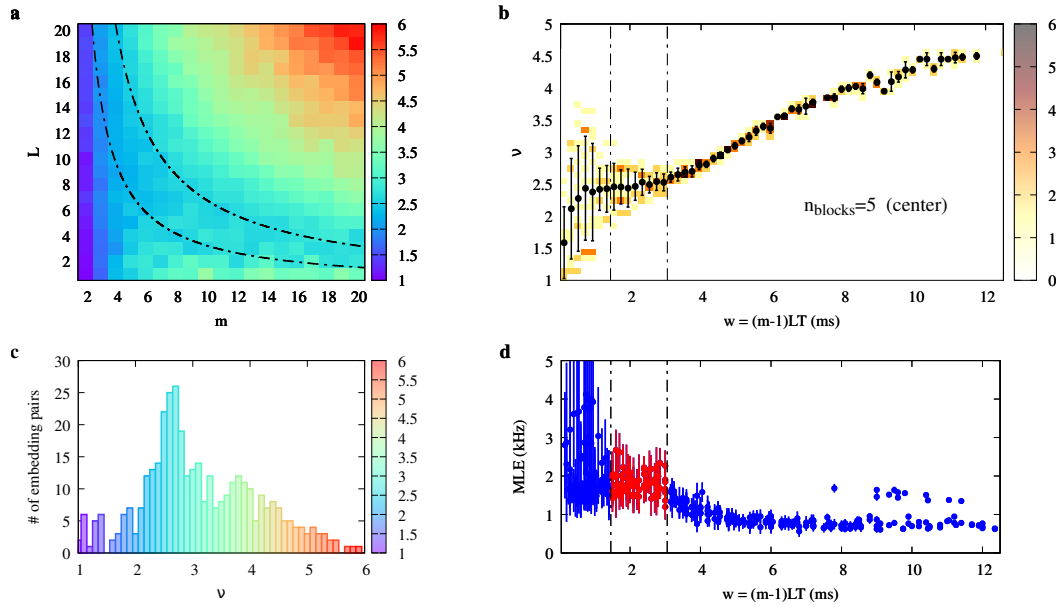


Figure 3.6: “Chasing chaos” analysis of the experimental W_3 time series obtained by setting $V_d = 0.05$ V with 5 coupled blocks. (a) Map of estimated correlation dimension ν vs. embedding pair (m, L) . The black, dash-dotted hyperbolae bound the region of uniform ν corresponding to the interval of the embedding window w highlighted in (b) and (d). (b) Sample joint distribution of (w, ν) for the ν -map in (a). Black dots and the related errorbars correspond to the expected value and the related uncertainty of ν for each given value (bin) of w . A uniformity region, highlighted by the dash-dotted vertical lines, is identified. (c) Histogram of the estimated ν . (d) Distribution of MLE as a function of w . Each point and the related uncertainty corresponds to the value assessed on an embedding pair by using the divergence rate method. A cluster of points, marked in red, can be identified in the uniformity region of (b), also highlighted here.

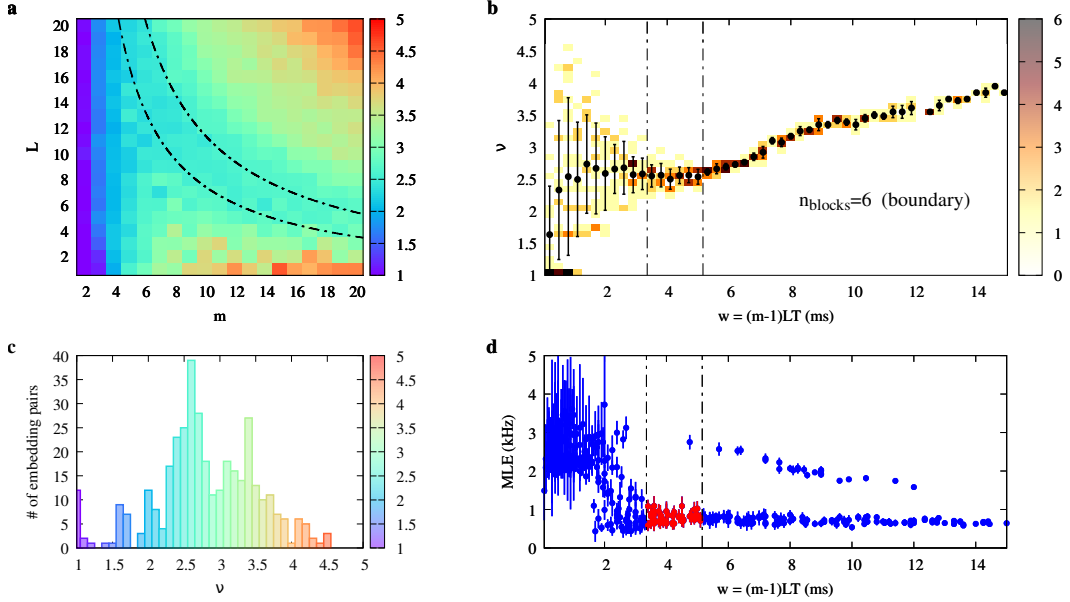


Figure 3.7: “Chasing chaos” analysis of the experimental W_1 time series obtained by setting $V_d = 0.05$ V with 6 coupled blocks. (a) Map of estimated correlation dimension ν vs. embedding pair (m, L) . The black, dash-dotted hyperbolae bound the region of uniform ν corresponding to the interval of the embedding window w highlighted in (b) and (d). (b) Sample joint distribution of (w, ν) for the ν -map in (a). Black dots and the related errorbars correspond to the expected value and the related uncertainty of ν for each given value (bin) of w . A uniformity region, highlighted by the dash-dotted vertical lines, is identified. (c) Histogram of the estimated ν . (d) Distribution of MLE as a function of w . Each point and the related uncertainty corresponds to the value assessed on an embedding pair by using the divergence rate method. A cluster of points, marked in red, can be identified in the uniformity region of (b), also highlighted here.

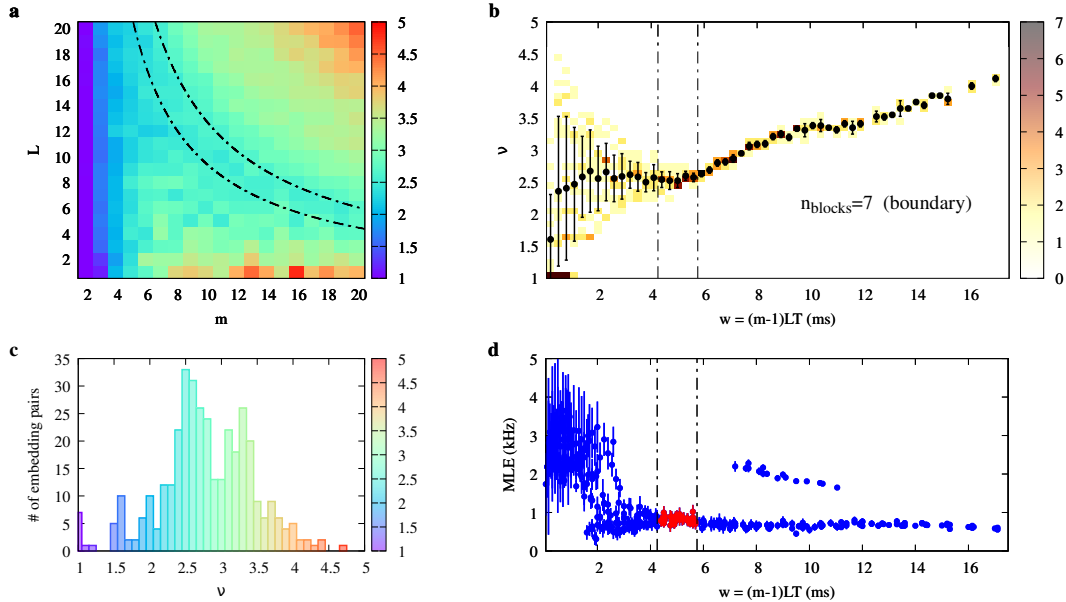


Figure 3.8: “Chasing chaos” analysis of the experimental W_1 time series obtained by setting $V_d = 0.05$ V with 7 coupled blocks. (a) Map of estimated correlation dimension ν vs. embedding pair (m, L) . The black, dash-dotted hyperbolae bound the region of uniform ν corresponding to the interval of the embedding window w highlighted in (b) and (d). (b) Sample joint distribution of (w, ν) for the ν -map in (a). Black dots and the related errorbars correspond to the expected value and the related uncertainty of ν for each given value (bin) of w . A uniformity region, highlighted by the dash-dotted vertical lines, is identified. (c) Histogram of the estimated ν . (d) Distribution of MLE as a function of w . Each point and the related uncertainty corresponds to the value assessed on an embedding pair by using the divergence rate method. A cluster of points, marked in red, can be identified in the uniformity region of (b), also highlighted here.

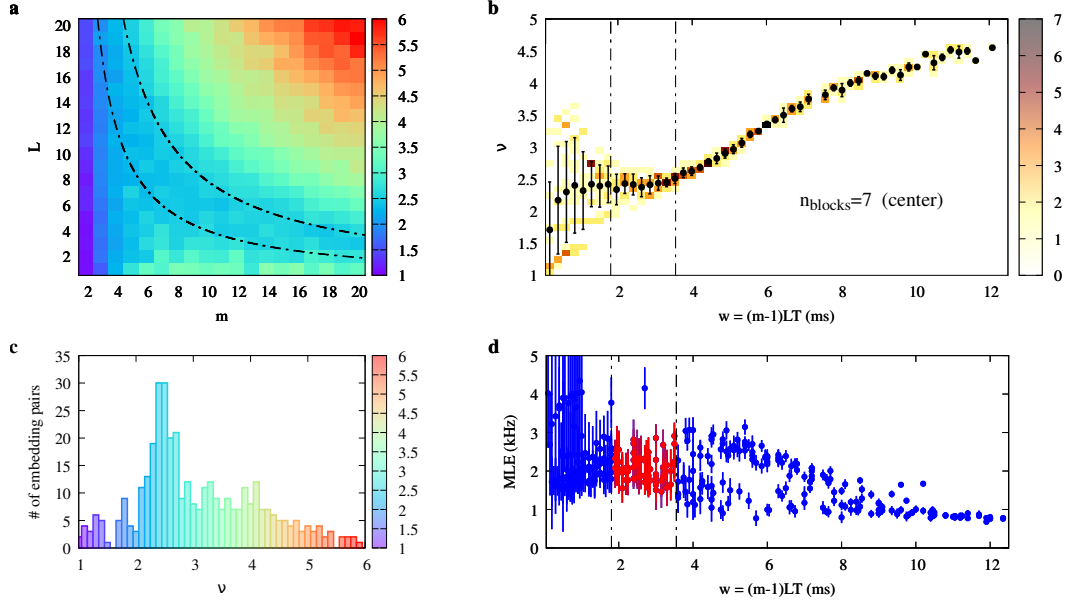


Figure 3.9: “Chasing chaos” analysis of the experimental W_4 time series obtained by setting $V_d = 0.05$ V with 7 coupled blocks. (a) Map of estimated correlation dimension ν vs. embedding pair (m, L) . The black, dash-dotted hyperbolae bound the region of uniform ν corresponding to the interval of the embedding window w highlighted in (b) and (d). (b) Sample joint distribution of (w, ν) for the ν -map in (a). Black dots and the related errorbars correspond to the expected value and the related uncertainty of ν for each given value (bin) of w . A uniformity region, highlighted by the dash-dotted vertical lines, is identified. (c) Histogram of the estimated ν . (d) Distribution of MLE as a function of w . Each point and the related uncertainty corresponds to the value assessed on an embedding pair by using the divergence rate method. A cluster of points, marked in red, can be identified in the uniformity region of (b), also highlighted here.

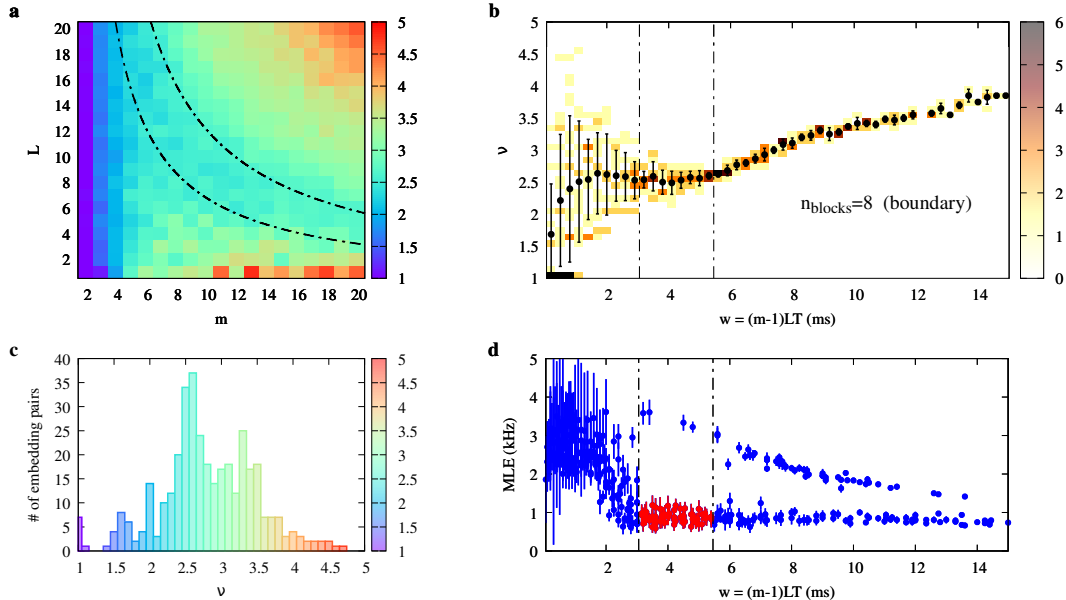


Figure 3.10: “Chasing chaos” analysis of the experimental W_1 time series obtained by setting $V_d = 0.05$ V with 8 coupled blocks. (a) Map of estimated correlation dimension ν vs. embedding pair (m, L) . The black, dash-dotted hyperbolae bound the region of uniform ν corresponding to the interval of the embedding window w highlighted in (b) and (d). (b) Sample joint distribution of (w, ν) for the ν -map in (a). Black dots and the related errorbars correspond to the expected value and the related uncertainty of ν for each given value (bin) of w . A uniformity region, highlighted by the dash-dotted vertical lines, is identified. (c) Histogram of the estimated ν . (d) Distribution of MLE as a function of w . Each point and the related uncertainty corresponds to the value assessed on an embedding pair by using the divergence rate method. A cluster of points, marked in red, can be identified in the uniformity region of (b), also highlighted here.

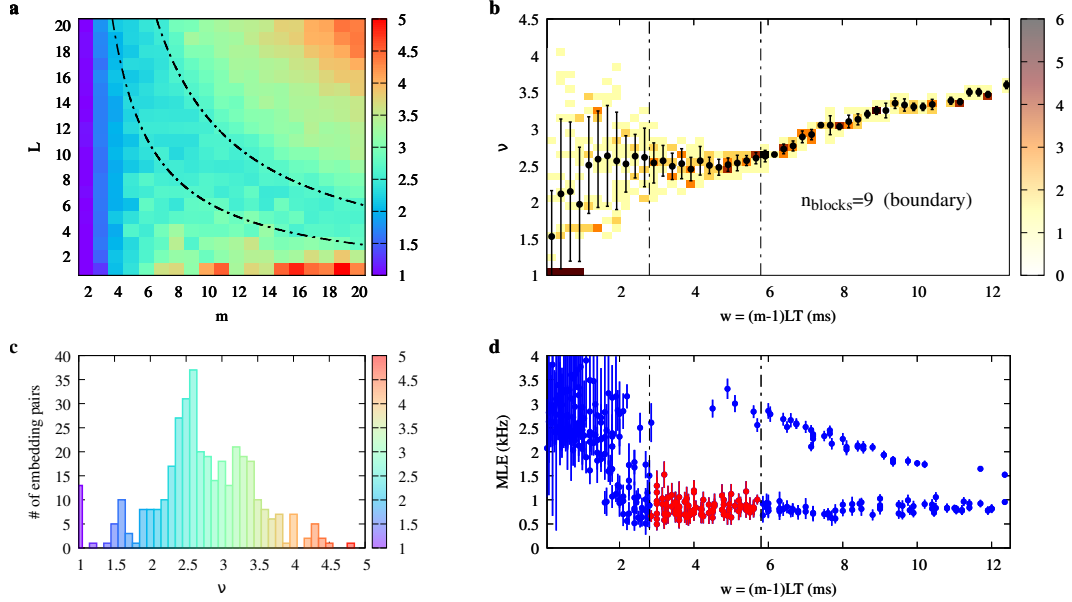


Figure 3.11: “Chasing chaos” analysis of the experimental W_1 time series obtained by setting $V_d = 0.05$ V with 9 coupled blocks. (a) Map of estimated correlation dimension ν vs. embedding pair (m, L) . The black, dash-dotted hyperbolae bound the region of uniform ν corresponding to the interval of the embedding window w highlighted in (b) and (d). (b) Sample joint distribution of (w, ν) for the ν -map in (a). Black dots and the related errobars correspond to the expected value and the related uncertainty of ν for each given value (bin) of w . A uniformity region, highlighted by the dash-dotted vertical lines, is identified. (c) Histogram of the estimated ν . (d) Distribution of MLE as a function of w . Each point and the related uncertainty corresponds to the value assessed on an embedding pair by using the divergence rate method. A cluster of points, marked in red, can be identified in the uniformity region of (b), also highlighted here.

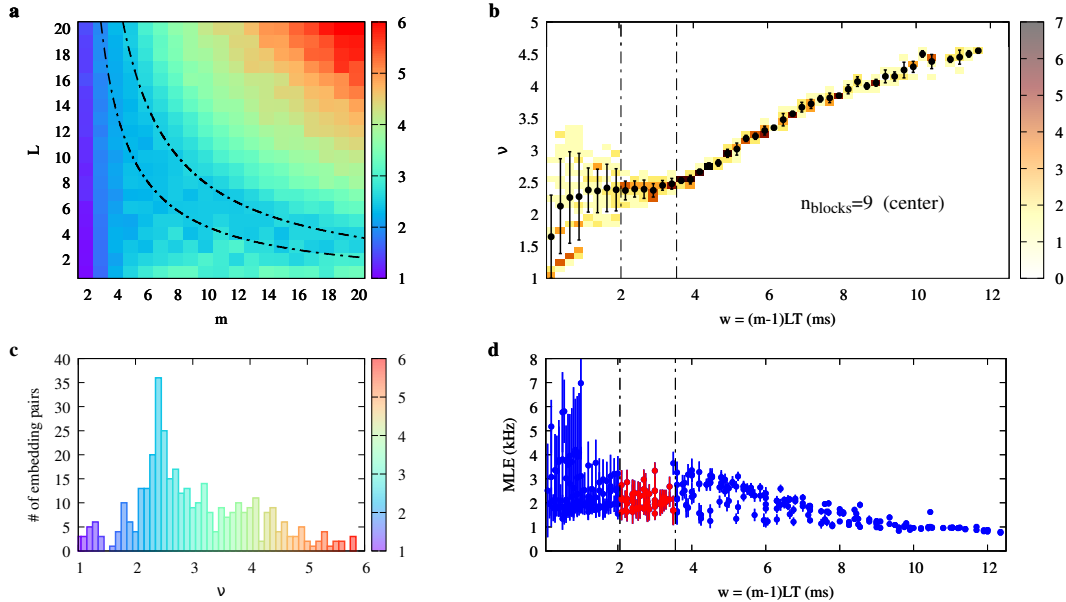


Figure 3.12: “Chasing chaos” analysis of the experimental W_5 time series obtained by setting $V_d = 0.05$ V with 9 coupled blocks. (a) Map of estimated correlation dimension ν vs. embedding pair (m, L) . The black, dash-dotted hyperbolae bound the region of uniform ν corresponding to the interval of the embedding window w highlighted in (b) and (d). (b) Sample joint distribution of (w, ν) for the ν -map in (a). Black dots and the related errorbars correspond to the expected value and the related uncertainty of ν for each given value (bin) of w . A uniformity region, highlighted by the dash-dotted vertical lines, is identified. (c) Histogram of the estimated ν . (d) Distribution of MLE as a function of w . Each point and the related uncertainty corresponds to the value assessed on an embedding pair by using the divergence rate method. A cluster of points, marked in red, can be identified in the uniformity region of (b), also highlighted here.

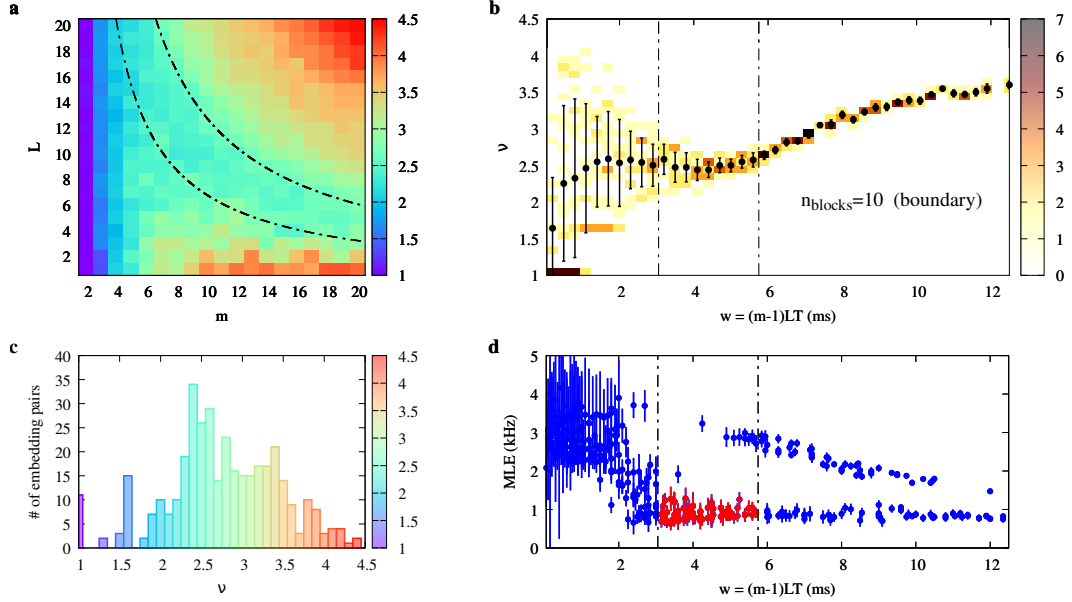


Figure 3.13: “Chasing chaos” analysis of the experimental W_1 time series obtained by setting $V_d = 0.05$ V with 10 coupled blocks. (a) Map of estimated correlation dimension ν vs. embedding pair (m, L) . The black, dash-dotted hyperbolae bound the region of uniform ν corresponding to the interval of the embedding window w highlighted in (b) and (d). (b) Sample joint distribution of (w, ν) for the ν -map in (a). Black dots and the related errorbars correspond to the expected value and the related uncertainty of ν for each given value (bin) of w . A uniformity region, highlighted by the dash-dotted vertical lines, is identified. (c) Histogram of the estimated ν . (d) Distribution of MLE as a function of w . Each point and the related uncertainty corresponds to the value assessed on an embedding pair by using the divergence rate method. A cluster of points, marked in red, can be identified in the uniformity region of (b), also highlighted here.

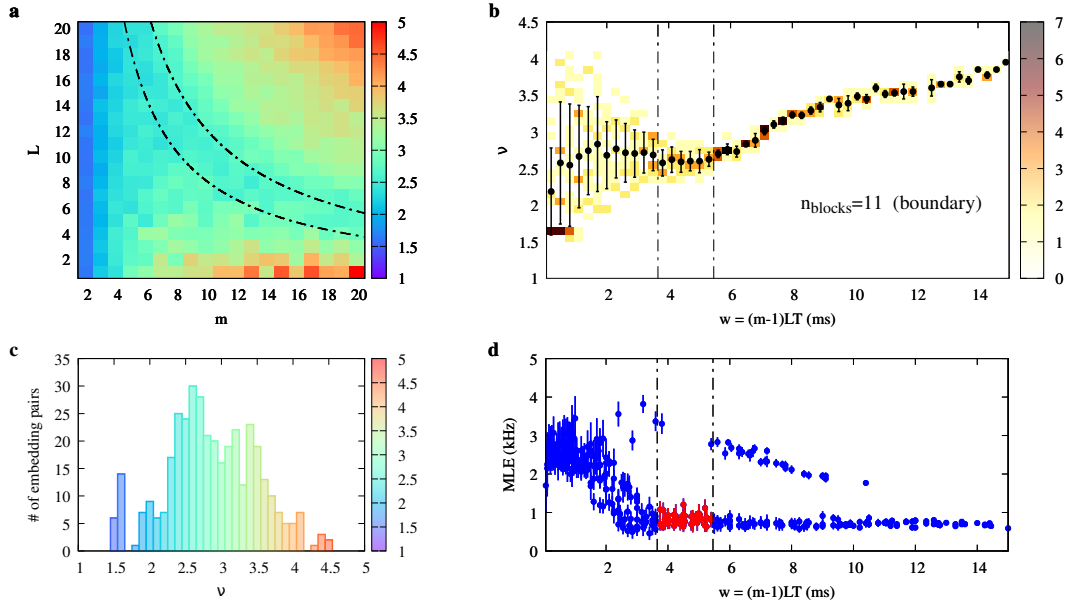


Figure 3.14: “Chasing chaos” analysis of the experimental W_1 time series obtained by setting $V_d = 0.05$ V with 11 coupled blocks. (a) Map of estimated correlation dimension ν vs. embedding pair (m, L) . The black, dash-dotted hyperbolae bound the region of uniform ν corresponding to the interval of the embedding window w highlighted in (b) and (d). (b) Sample joint distribution of (w, ν) for the ν -map in (a). Black dots and the related errorbars correspond to the expected value and the related uncertainty of ν for each given value (bin) of w . A uniformity region, highlighted by the dash-dotted vertical lines, is identified. (c) Histogram of the estimated ν . (d) Distribution of MLE as a function of w . Each point and the related uncertainty corresponds to the value assessed on an embedding pair by using the divergence rate method. A cluster of points, marked in red, can be identified in the uniformity region of (b), also highlighted here.

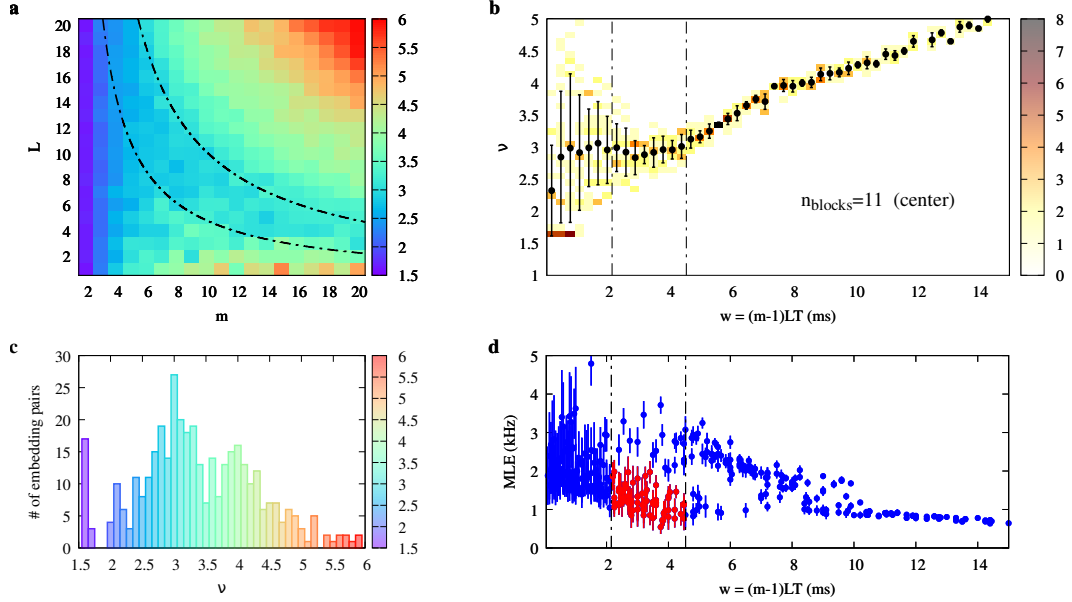


Figure 3.15: “Chasing chaos” analysis of the experimental W_6 time series obtained by setting $V_d = 0.05$ V with 11 coupled blocks. (a) Map of estimated correlation dimension ν vs. embedding pair (m, L) . The black, dash-dotted hyperbolae bound the region of uniform ν corresponding to the interval of the embedding window w highlighted in (b) and (d). (b) Sample joint distribution of (w, ν) for the ν -map in (a). Black dots and the related errobars correspond to the expected value and the related uncertainty of ν for each given value (bin) of w . A uniformity region, highlighted by the dash-dotted vertical lines, is identified. (c) Histogram of the estimated ν . (d) Distribution of MLE as a function of w . Each point and the related uncertainty corresponds to the value assessed on an embedding pair by using the divergence rate method. A cluster of points, marked in red, can be identified in the uniformity region of (b), also highlighted here.

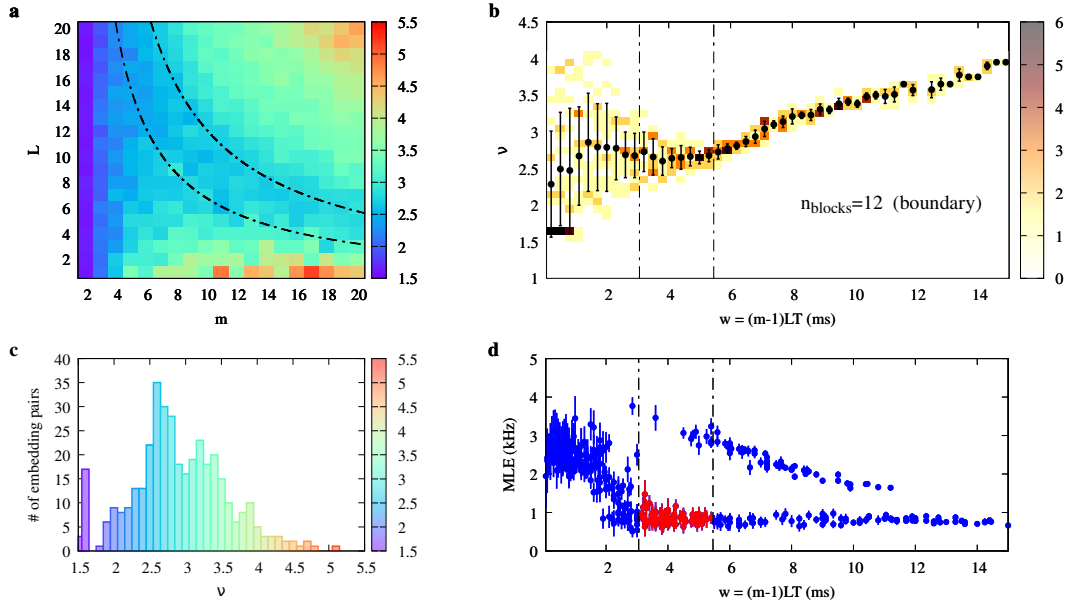


Figure 3.16: “Chasing chaos” analysis of the experimental W_1 time series obtained by setting $V_d = 0.05$ V with 12 coupled blocks. (a) Map of estimated correlation dimension ν vs. embedding pair (m, L) . The black, dash-dotted hyperbolae bound the region of uniform ν corresponding to the interval of the embedding window w highlighted in (b) and (d). (b) Sample joint distribution of (w, ν) for the ν -map in (a). Black dots and the related errorbars correspond to the expected value and the related uncertainty of ν for each given value (bin) of w . A uniformity region, highlighted by the dash-dotted vertical lines, is identified. (c) Histogram of the estimated ν . (d) Distribution of MLE as a function of w . Each point and the related uncertainty corresponds to the value assessed on an embedding pair by using the divergence rate method. A cluster of points, marked in red, can be identified in the uniformity region of (b), also highlighted here.

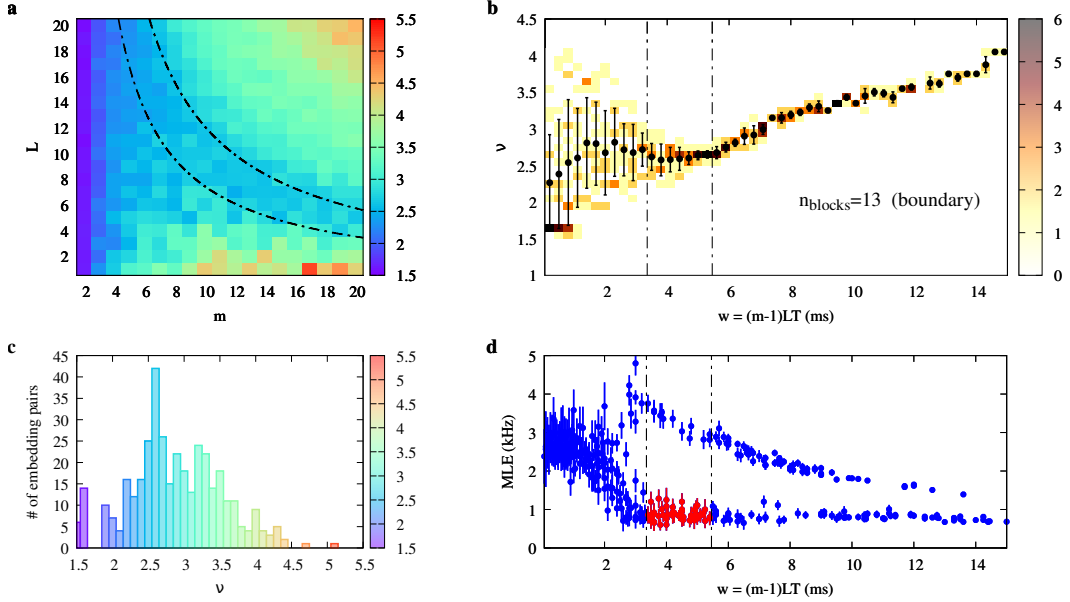


Figure 3.17: “Chasing chaos” analysis of the experimental W_1 time series obtained by setting $V_d = 0.05$ V with 13 coupled blocks. (a) Map of estimated correlation dimension ν vs. embedding pair (m, L) . The black, dash-dotted hyperbolae bound the region of uniform ν corresponding to the interval of the embedding window w highlighted in (b) and (d). (b) Sample joint distribution of (w, ν) for the ν -map in (a). Black dots and the related errobars correspond to the expected value and the related uncertainty of ν for each given value (bin) of w . A uniformity region, highlighted by the dash-dotted vertical lines, is identified. (c) Histogram of the estimated ν . (d) Distribution of MLE as a function of w . Each point and the related uncertainty corresponds to the value assessed on an embedding pair by using the divergence rate method. A cluster of points, marked in red, can be identified in the uniformity region of (b), also highlighted here.

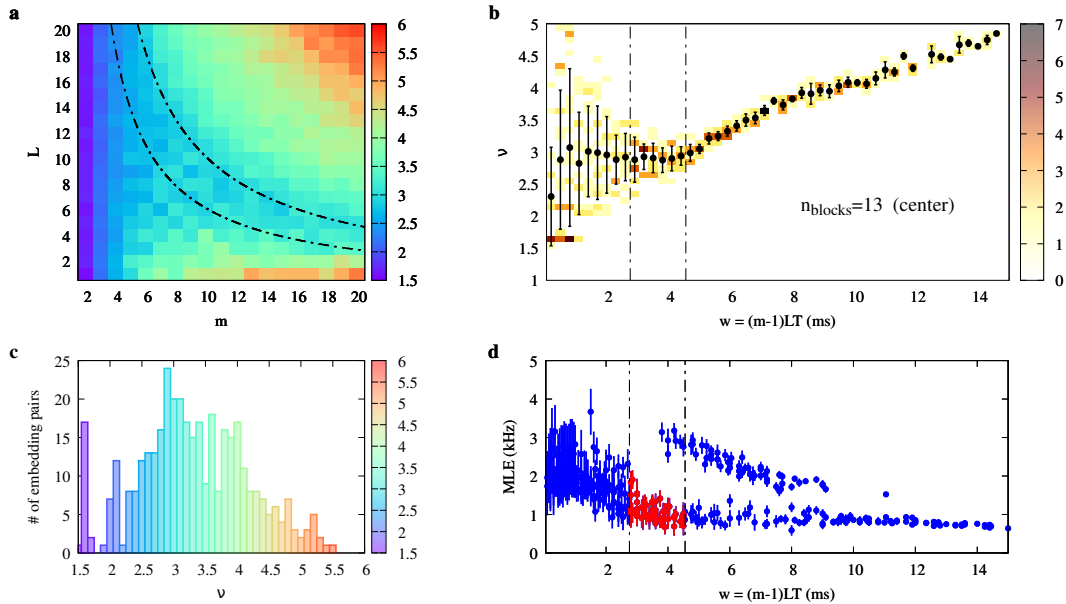


Figure 3.18: “Chasing chaos” analysis of the experimental W_7 time series obtained by setting $V_d = 0.05$ V with 13 coupled blocks. (a) Map of estimated correlation dimension ν vs. embedding pair (m, L) . The black, dash-dotted hyperbolae bound the region of uniform ν corresponding to the interval of the embedding window w highlighted in (b) and (d). (b) Sample joint distribution of (w, ν) for the ν -map in (a). Black dots and the related errorbars correspond to the expected value and the related uncertainty of ν for each given value (bin) of w . A uniformity region, highlighted by the dash-dotted vertical lines, is identified. (c) Histogram of the estimated ν . (d) Distribution of MLE as a function of w . Each point and the related uncertainty corresponds to the value assessed on an embedding pair by using the divergence rate method. A cluster of points, marked in red, can be identified in the uniformity region of (b), also highlighted here.

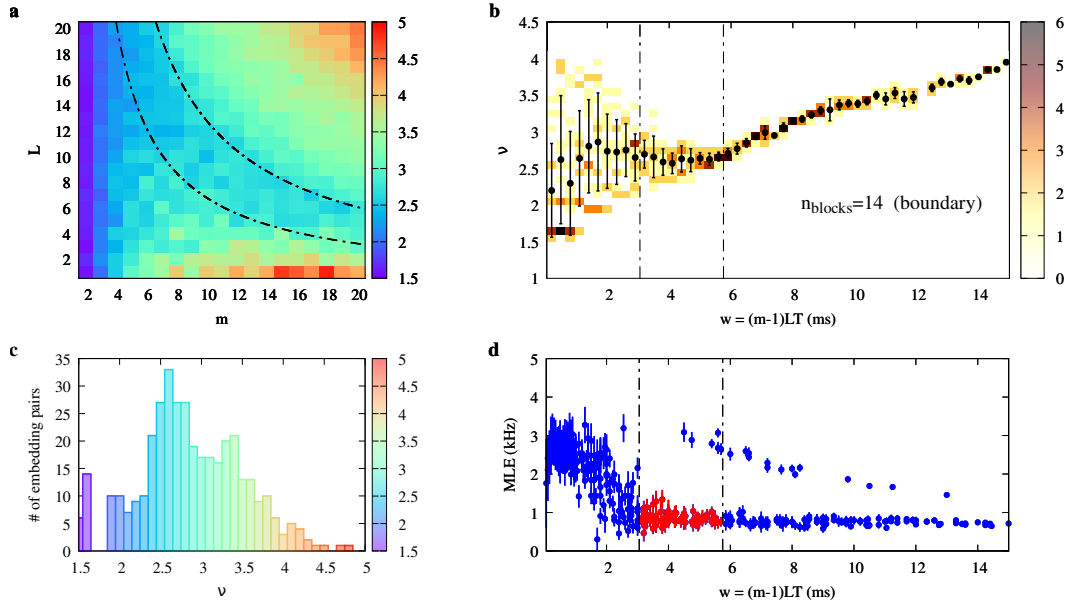


Figure 3.19: “Chasing chaos” analysis of the experimental W_1 time series obtained by setting $V_d = 0.05$ V with 14 coupled blocks. (a) Map of estimated correlation dimension ν vs. embedding pair (m, L) . The black, dash-dotted hyperbolae bound the region of uniform ν corresponding to the interval of the embedding window w highlighted in (b) and (d). (b) Sample joint distribution of (w, ν) for the ν -map in (a). Black dots and the related errorbars correspond to the expected value and the related uncertainty of ν for each given value (bin) of w . A uniformity region, highlighted by the dash-dotted vertical lines, is identified. (c) Histogram of the estimated ν . (d) Distribution of MLE as a function of w . Each point and the related uncertainty corresponds to the value assessed on an embedding pair by using the divergence rate method. A cluster of points, marked in red, can be identified in the uniformity region of (b), also highlighted here.

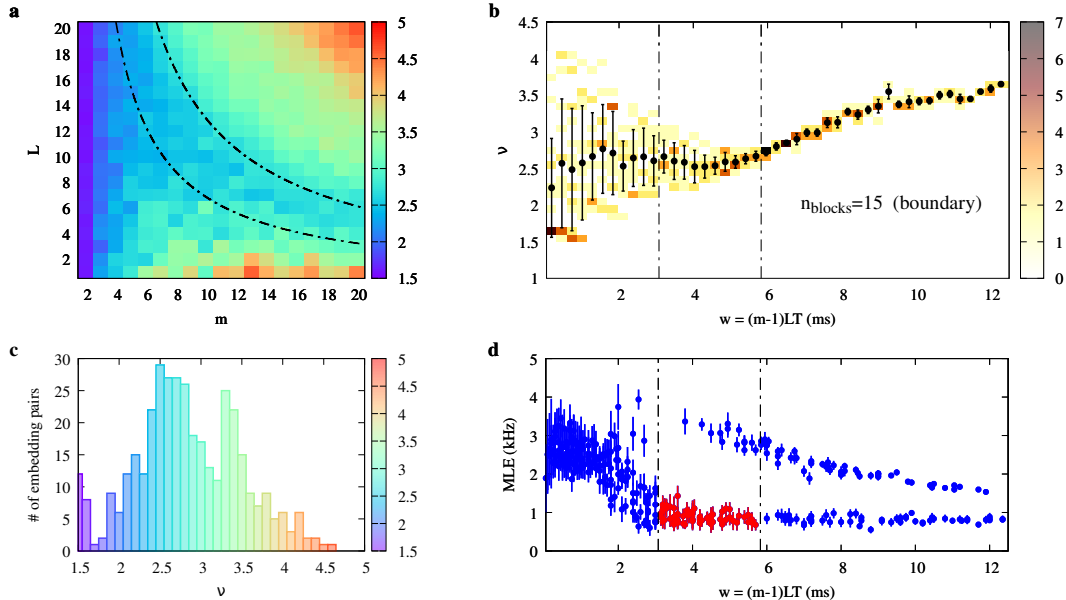


Figure 3.20: “Chasing chaos” analysis of the experimental W_1 time series obtained by setting $V_d = 0.05$ V with 15 coupled blocks. (a) Map of estimated correlation dimension ν vs. embedding pair (m, L) . The black, dash-dotted hyperbolae bound the region of uniform ν corresponding to the interval of the embedding window w highlighted in (b) and (d). (b) Sample joint distribution of (w, ν) for the ν -map in (a). Black dots and the related errorbars correspond to the expected value and the related uncertainty of ν for each given value (bin) of w . A uniformity region, highlighted by the dash-dotted vertical lines, is identified. (c) Histogram of the estimated ν . (d) Distribution of MLE as a function of w . Each point and the related uncertainty corresponds to the value assessed on an embedding pair by using the divergence rate method. A cluster of points, marked in red, can be identified in the uniformity region of (b), also highlighted here.

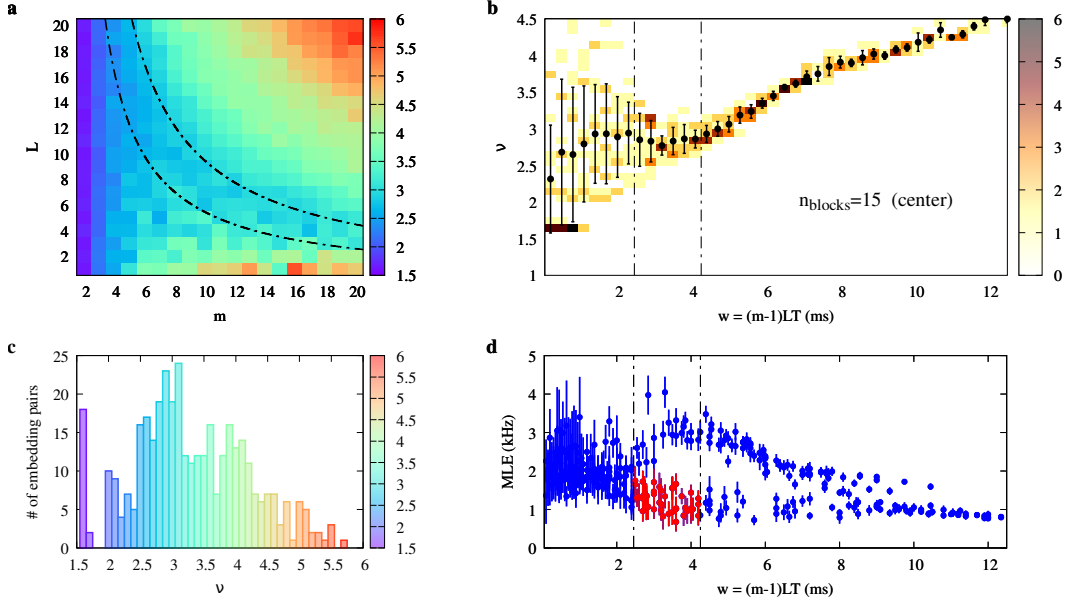


Figure 3.21: “Chasing chaos” analysis of the experimental W_8 time series obtained by setting $V_d = 0.05$ V with 15 coupled blocks. (a) Map of estimated correlation dimension ν vs. embedding pair (m, L) . The black, dash-dotted hyperbolae bound the region of uniform ν corresponding to the interval of the embedding window w highlighted in (b) and (d). (b) Sample joint distribution of (w, ν) for the ν -map in (a). Black dots and the related errorbars correspond to the expected value and the related uncertainty of ν for each given value (bin) of w . A uniformity region, highlighted by the dash-dotted vertical lines, is identified. (c) Histogram of the estimated ν . (d) Distribution of MLE as a function of w . Each point and the related uncertainty corresponds to the value assessed on an embedding pair by using the divergence rate method. A cluster of points, marked in red, can be identified in the uniformity region of (b), also highlighted here.

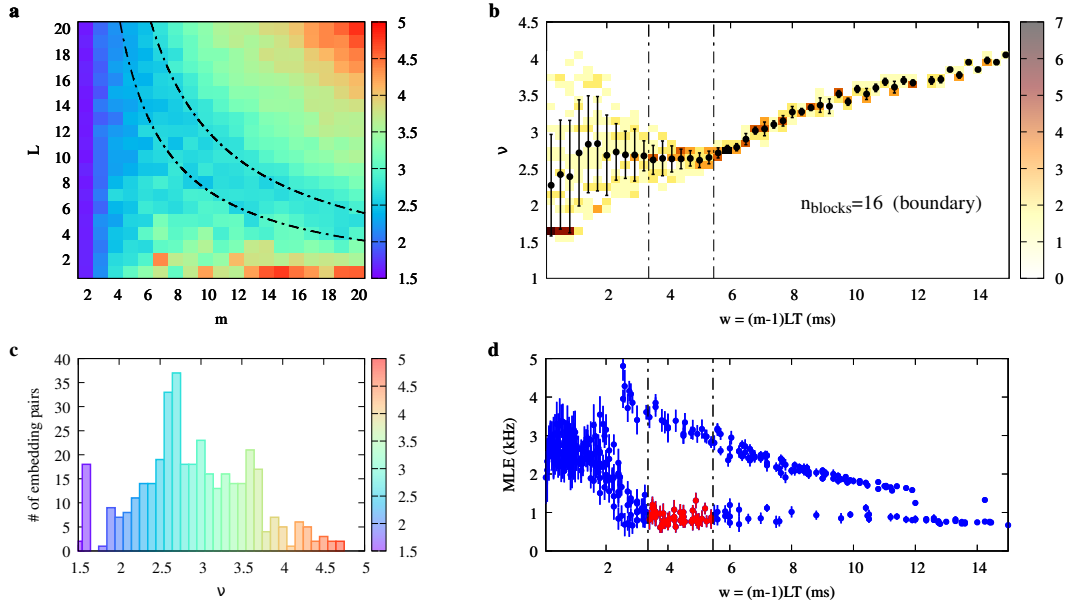


Figure 3.22: “Chasing chaos” analysis of the experimental W_1 time series obtained by setting $V_d = 0.05$ V with 16 coupled blocks. (a) Map of estimated correlation dimension ν vs. embedding pair (m, L) . The black, dash-dotted hyperbolae bound the region of uniform ν corresponding to the interval of the embedding window w highlighted in (b) and (d). (b) Sample joint distribution of (w, ν) for the ν -map in (a). Black dots and the related errorbars correspond to the expected value and the related uncertainty of ν for each given value (bin) of w . A uniformity region, highlighted by the dash-dotted vertical lines, is identified. (c) Histogram of the estimated ν . (d) Distribution of MLE as a function of w . Each point and the related uncertainty corresponds to the value assessed on an embedding pair by using the divergence rate method. A cluster of points, marked in red, can be identified in the uniformity region of (b), also highlighted here.

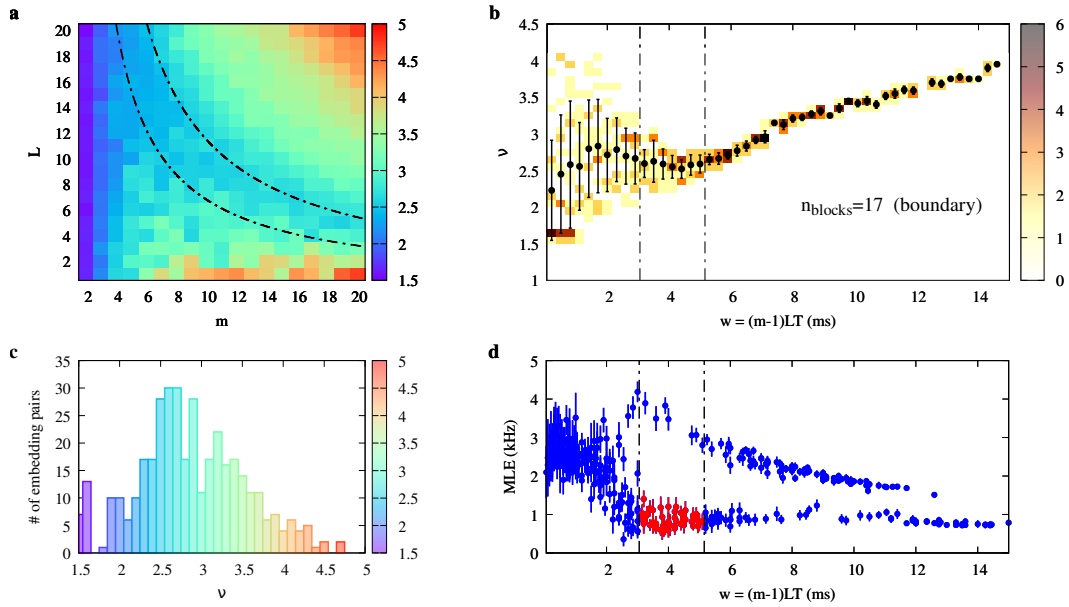


Figure 3.23: “Chasing chaos” analysis of the experimental W_1 time series obtained by setting $V_d = 0.05$ V with 17 coupled blocks. (a) Map of estimated correlation dimension ν vs. embedding pair (m, L) . The black, dash-dotted hyperbolae bound the region of uniform ν corresponding to the interval of the embedding window w highlighted in (b) and (d). (b) Sample joint distribution of (w, ν) for the ν -map in (a). Black dots and the related errorbars correspond to the expected value and the related uncertainty of ν for each given value (bin) of w . A uniformity region, highlighted by the dash-dotted vertical lines, is identified. (c) Histogram of the estimated ν . (d) Distribution of MLE as a function of w . Each point and the related uncertainty corresponds to the value assessed on an embedding pair by using the divergence rate method. A cluster of points, marked in red, can be identified in the uniformity region of (b), also highlighted here.

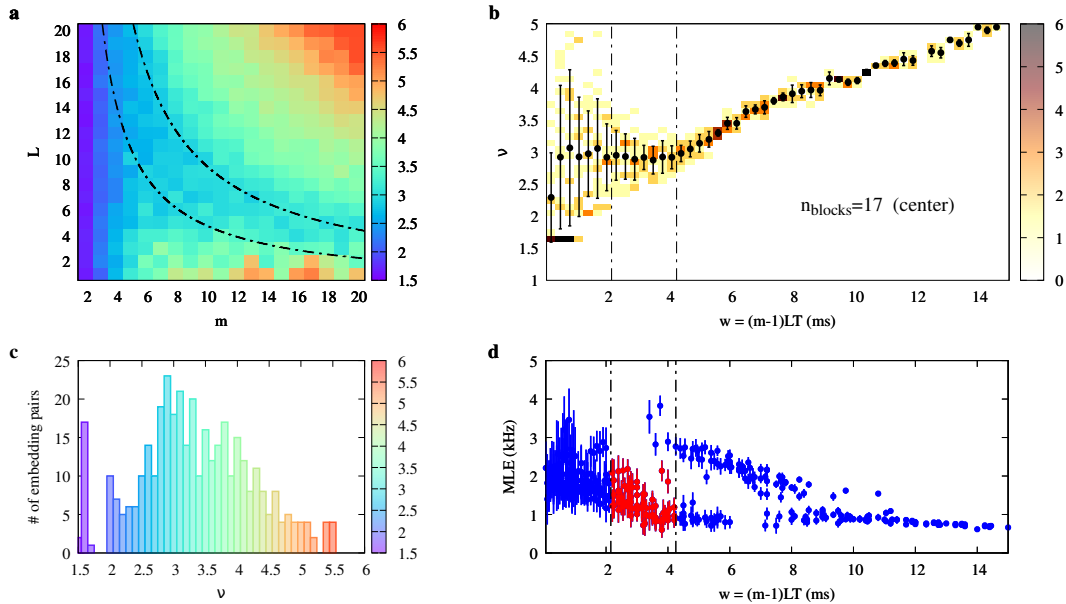


Figure 3.24: “Chasing chaos” analysis of the experimental W_9 time series obtained by setting $V_d = 0.05$ V with 17 coupled blocks. (a) Map of estimated correlation dimension ν vs. embedding pair (m, L) . The black, dash-dotted hyperbolae bound the region of uniform ν corresponding to the interval of the embedding window w highlighted in (b) and (d). (b) Sample joint distribution of (w, ν) for the ν -map in (a). Black dots and the related errorbars correspond to the expected value and the related uncertainty of ν for each given value (bin) of w . A uniformity region, highlighted by the dash-dotted vertical lines, is identified. (c) Histogram of the estimated ν . (d) Distribution of MLE as a function of w . Each point and the related uncertainty corresponds to the value assessed on an embedding pair by using the divergence rate method. A cluster of points, marked in red, can be identified in the uniformity region of (b), also highlighted here.

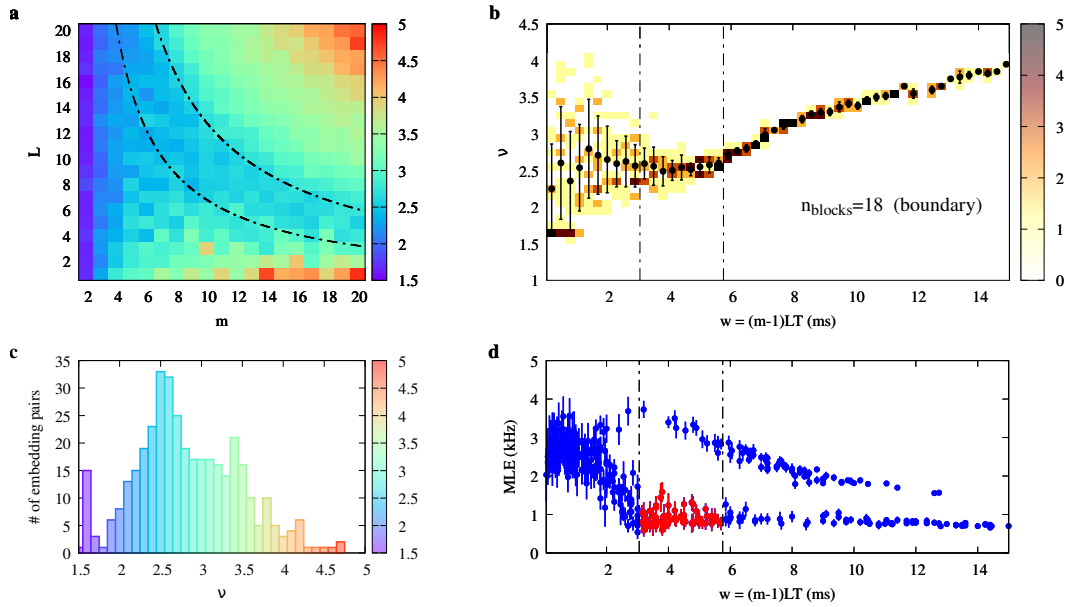


Figure 3.25: “Chasing chaos” analysis of the experimental W_1 time series obtained by setting $V_d = 0.05$ V with 18 coupled blocks. (a) Map of estimated correlation dimension ν vs. embedding pair (m, L) . The black, dash-dotted hyperbolae bound the region of uniform ν corresponding to the interval of the embedding window w highlighted in (b) and (d). (b) Sample joint distribution of (w, ν) for the ν -map in (a). Black dots and the related errorbars correspond to the expected value and the related uncertainty of ν for each given value (bin) of w . A uniformity region, highlighted by the dash-dotted vertical lines, is identified. (c) Histogram of the estimated ν . (d) Distribution of MLE as a function of w . Each point and the related uncertainty corresponds to the value assessed on an embedding pair by using the divergence rate method. A cluster of points, marked in red, can be identified in the uniformity region of (b), also highlighted here.

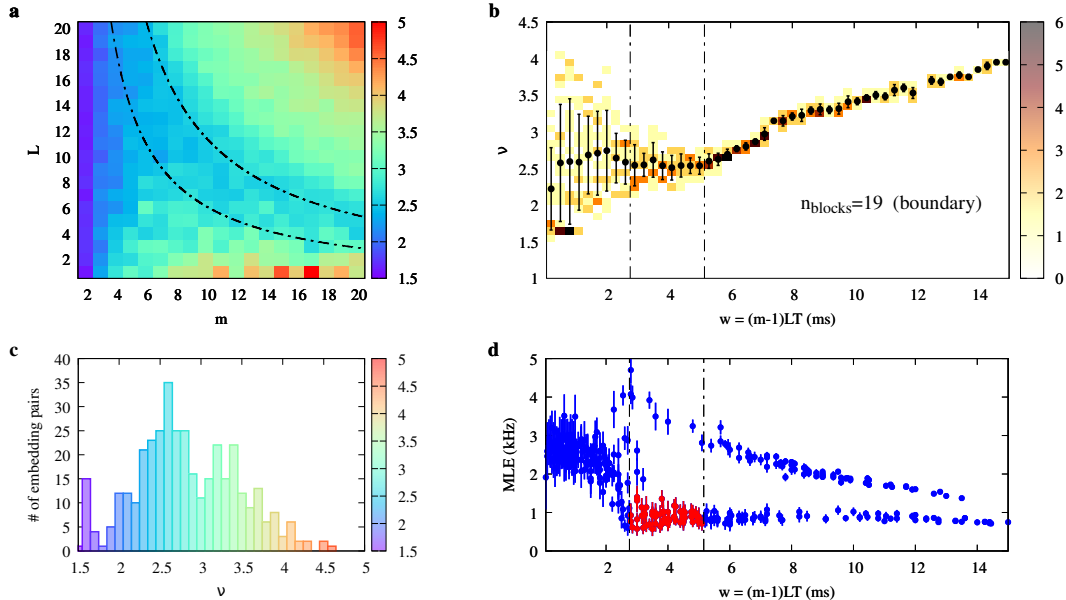


Figure 3.26: “Chasing chaos” analysis of the experimental W_1 time series obtained by setting $V_d = 0.05$ V with 19 coupled blocks. (a) Map of estimated correlation dimension ν vs. embedding pair (m, L) . The black, dash-dotted hyperbolae bound the region of uniform ν corresponding to the interval of the embedding window w highlighted in (b) and (d). (b) Sample joint distribution of (w, ν) for the ν -map in (a). Black dots and the related errorbars correspond to the expected value and the related uncertainty of ν for each given value (bin) of w . A uniformity region, highlighted by the dash-dotted vertical lines, is identified. (c) Histogram of the estimated ν . (d) Distribution of MLE as a function of w . Each point and the related uncertainty corresponds to the value assessed on an embedding pair by using the divergence rate method. A cluster of points, marked in red, can be identified in the uniformity region of (b), also highlighted here.

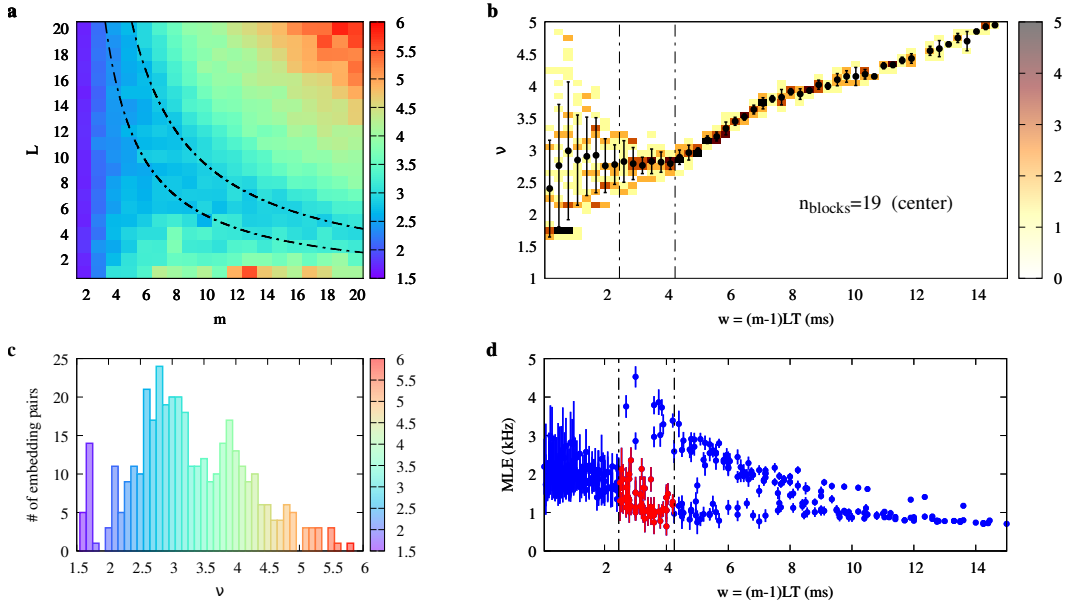


Figure 3.27: “Chasing chaos” analysis of the experimental W_{10} time series obtained by setting $V_d = 0.05$ V with 19 coupled blocks. (a) Map of estimated correlation dimension ν vs. embedding pair (m, L) . The black, dash-dotted hyperbolae bound the region of uniform ν corresponding to the interval of the embedding window w highlighted in (b) and (d). (b) Sample joint distribution of (w, ν) for the ν -map in (a). Black dots and the related errorbars correspond to the expected value and the related uncertainty of ν for each given value (bin) of w . A uniformity region, highlighted by the dash-dotted vertical lines, is identified. (c) Histogram of the estimated ν . (d) Distribution of MLE as a function of w . Each point and the related uncertainty corresponds to the value assessed on an embedding pair by using the divergence rate method. A cluster of points, marked in red, can be identified in the uniformity region of (b), also highlighted here.

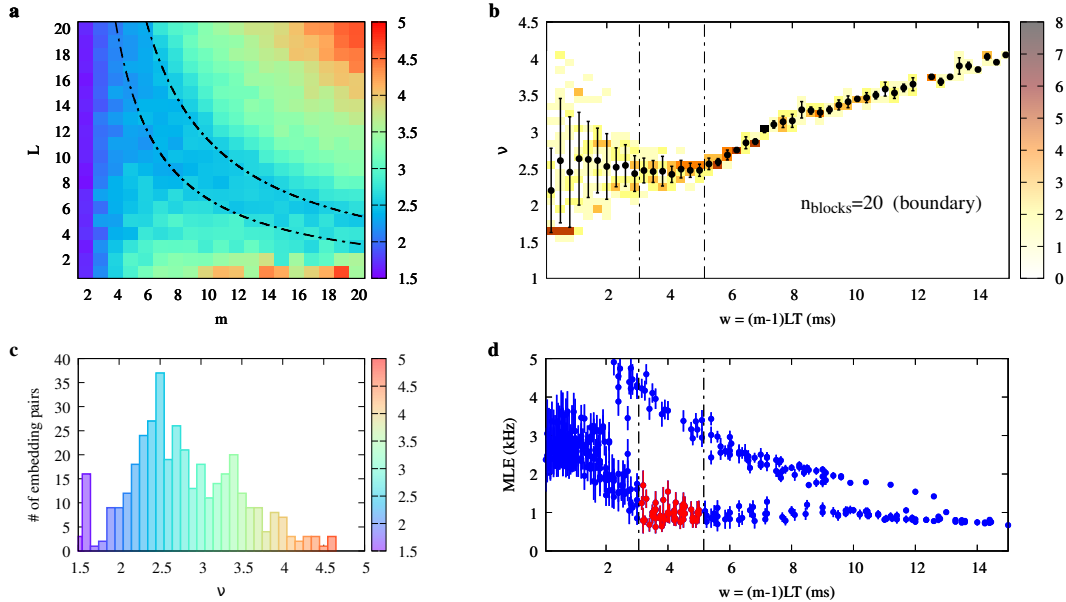


Figure 3.28: “Chasing chaos” analysis of the experimental W_1 time series obtained by setting $V_d = 0.05$ V with 20 coupled blocks. (a) Map of estimated correlation dimension ν vs. embedding pair (m, L) . The black, dash-dotted hyperbolae bound the region of uniform ν corresponding to the interval of the embedding window w highlighted in (b) and (d). (b) Sample joint distribution of (w, ν) for the ν -map in (a). Black dots and the related errorbars correspond to the expected value and the related uncertainty of ν for each given value (bin) of w . A uniformity region, highlighted by the dash-dotted vertical lines, is identified. (c) Histogram of the estimated ν . (d) Distribution of MLE as a function of w . Each point and the related uncertainty corresponds to the value assessed on an embedding pair by using the divergence rate method. A cluster of points, marked in red, can be identified in the uniformity region of (b), also highlighted here.

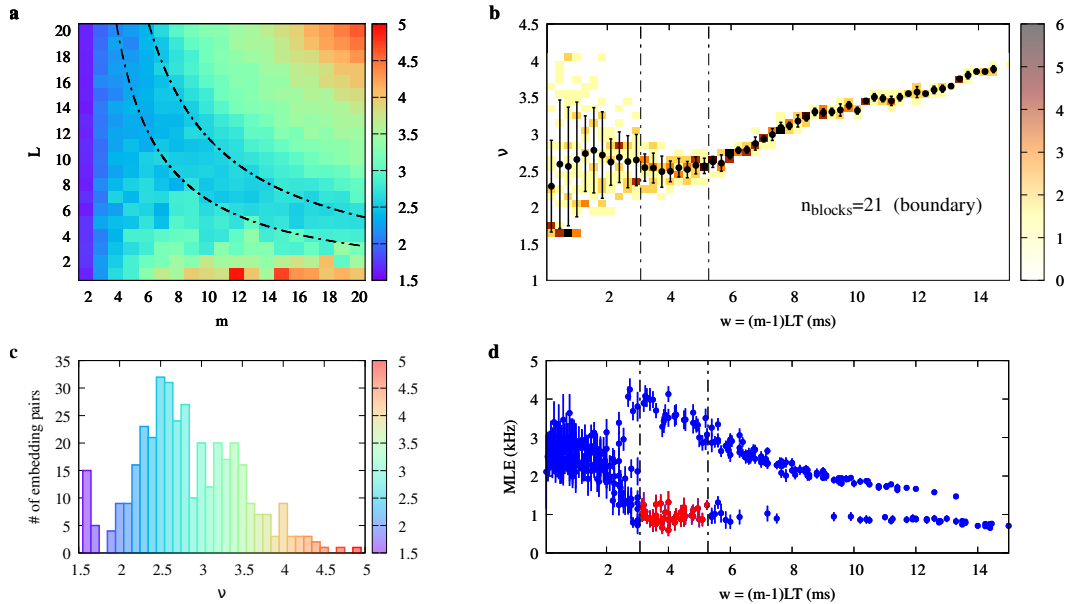


Figure 3.29: “Chasing chaos” analysis of the experimental W_1 time series obtained by setting $V_d = 0.05$ V with 21 coupled blocks. (a) Map of estimated correlation dimension ν vs. embedding pair (m, L) . The black, dash-dotted hyperbolae bound the region of uniform ν corresponding to the interval of the embedding window w highlighted in (b) and (d). (b) Sample joint distribution of (w, ν) for the ν -map in (a). Black dots and the related errorbars correspond to the expected value and the related uncertainty of ν for each given value (bin) of w . A uniformity region, highlighted by the dash-dotted vertical lines, is identified. (c) Histogram of the estimated ν . (d) Distribution of MLE as a function of w . Each point and the related uncertainty corresponds to the value assessed on an embedding pair by using the divergence rate method. A cluster of points, marked in red, can be identified in the uniformity region of (b), also highlighted here.

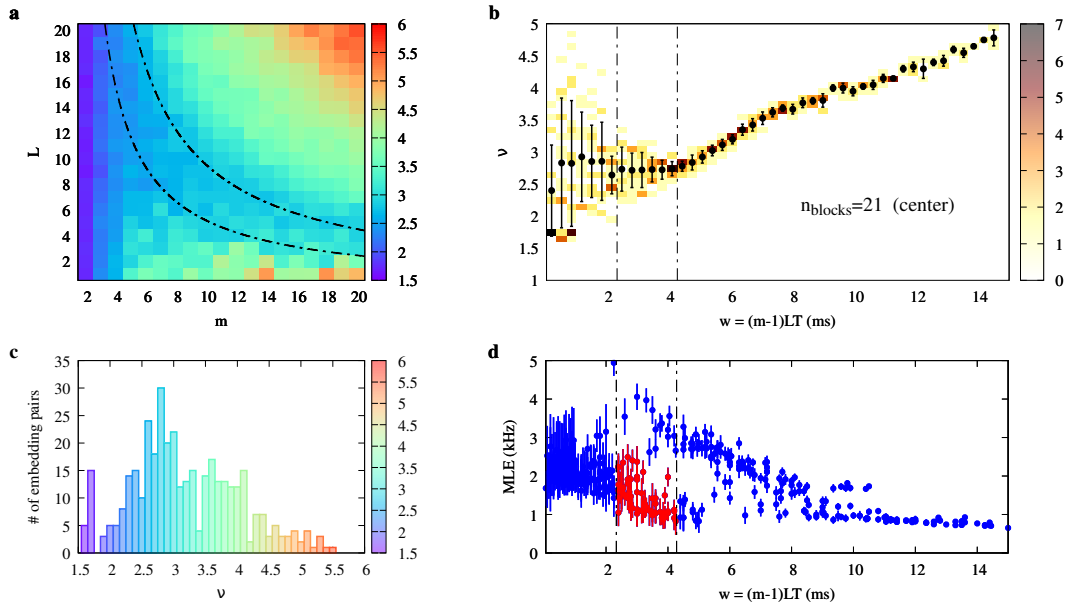


Figure 3.30: “Chasing chaos” analysis of the experimental W_{11} time series obtained by setting $V_d = 0.05$ V with 21 coupled blocks. (a) Map of estimated correlation dimension ν vs. embedding pair (m, L) . The black, dash-dotted hyperbolae bound the region of uniform ν corresponding to the interval of the embedding window w highlighted in (b) and (d). (b) Sample joint distribution of (w, ν) for the ν -map in (a). Black dots and the related errorbars correspond to the expected value and the related uncertainty of ν for each given value (bin) of w . A uniformity region, highlighted by the dash-dotted vertical lines, is identified. (c) Histogram of the estimated ν . (d) Distribution of MLE as a function of w . Each point and the related uncertainty corresponds to the value assessed on an embedding pair by using the divergence rate method. A cluster of points, marked in red, can be identified in the uniformity region of (b), also highlighted here.

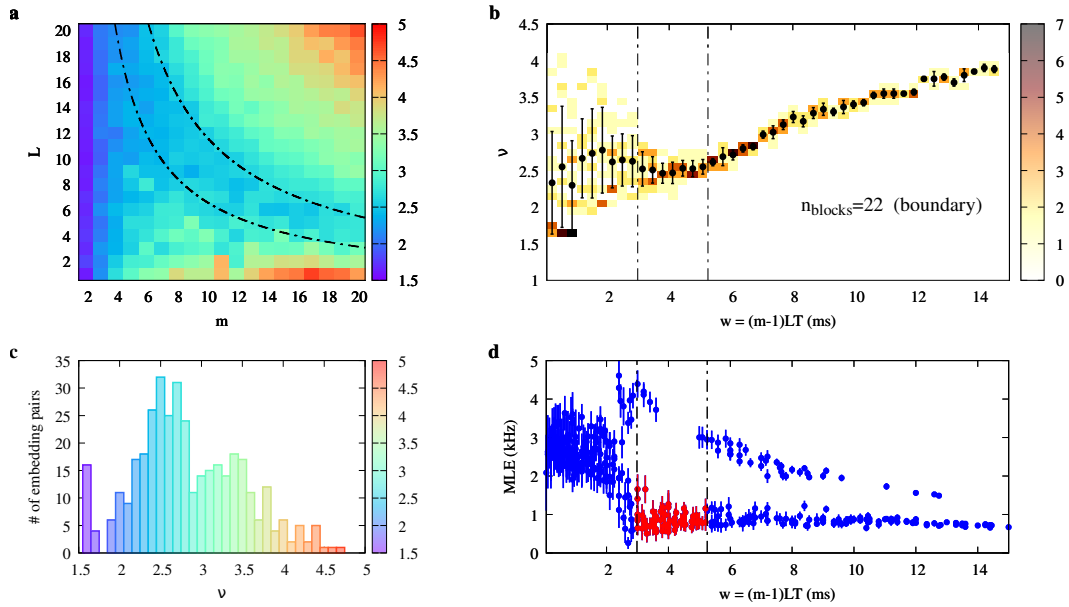


Figure 3.31: “Chasing chaos” analysis of the experimental W_1 time series obtained by setting $V_d = 0.05$ V with 22 coupled blocks. (a) Map of estimated correlation dimension ν vs. embedding pair (m, L) . The black, dash-dotted hyperbolae bound the region of uniform ν corresponding to the interval of the embedding window w highlighted in (b) and (d). (b) Sample joint distribution of (w, ν) for the ν -map in (a). Black dots and the related errorbars correspond to the expected value and the related uncertainty of ν for each given value (bin) of w . A uniformity region, highlighted by the dash-dotted vertical lines, is identified. (c) Histogram of the estimated ν . (d) Distribution of MLE as a function of w . Each point and the related uncertainty corresponds to the value assessed on an embedding pair by using the divergence rate method. A cluster of points, marked in red, can be identified in the uniformity region of (b), also highlighted here.

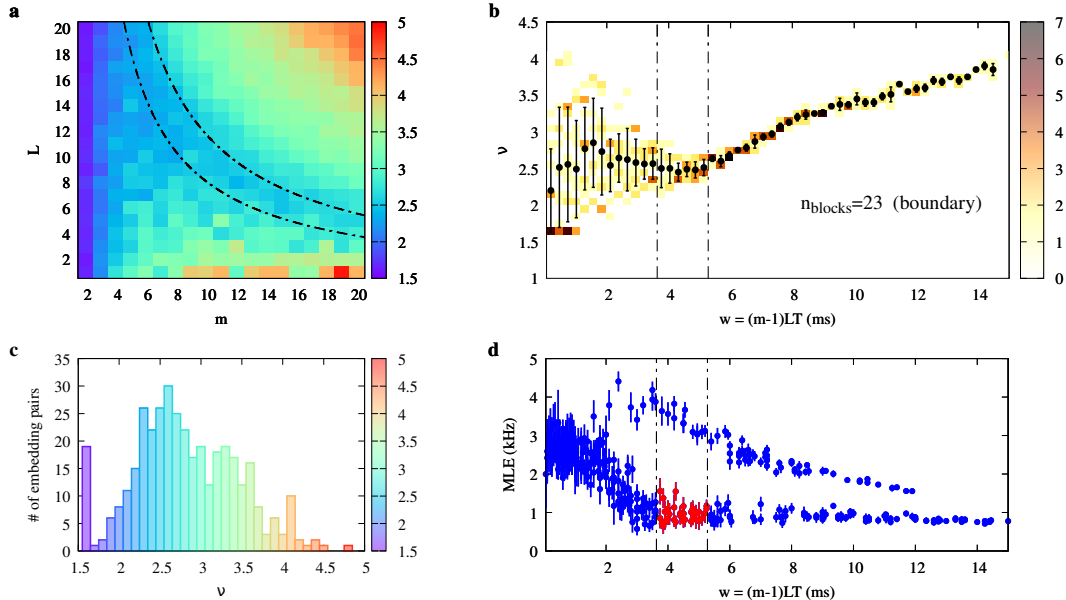


Figure 3.32: “Chasing chaos” analysis of the experimental W_1 time series obtained by setting $V_d = 0.05$ V with 23 coupled blocks. (a) Map of estimated correlation dimension ν vs. embedding pair (m, L) . The black, dash-dotted hyperbolae bound the region of uniform ν corresponding to the interval of the embedding window w highlighted in (b) and (d). (b) Sample joint distribution of (w, ν) for the ν -map in (a). Black dots and the related errorbars correspond to the expected value and the related uncertainty of ν for each given value (bin) of w . A uniformity region, highlighted by the dash-dotted vertical lines, is identified. (c) Histogram of the estimated ν . (d) Distribution of MLE as a function of w . Each point and the related uncertainty corresponds to the value assessed on an embedding pair by using the divergence rate method. A cluster of points, marked in red, can be identified in the uniformity region of (b), also highlighted here.

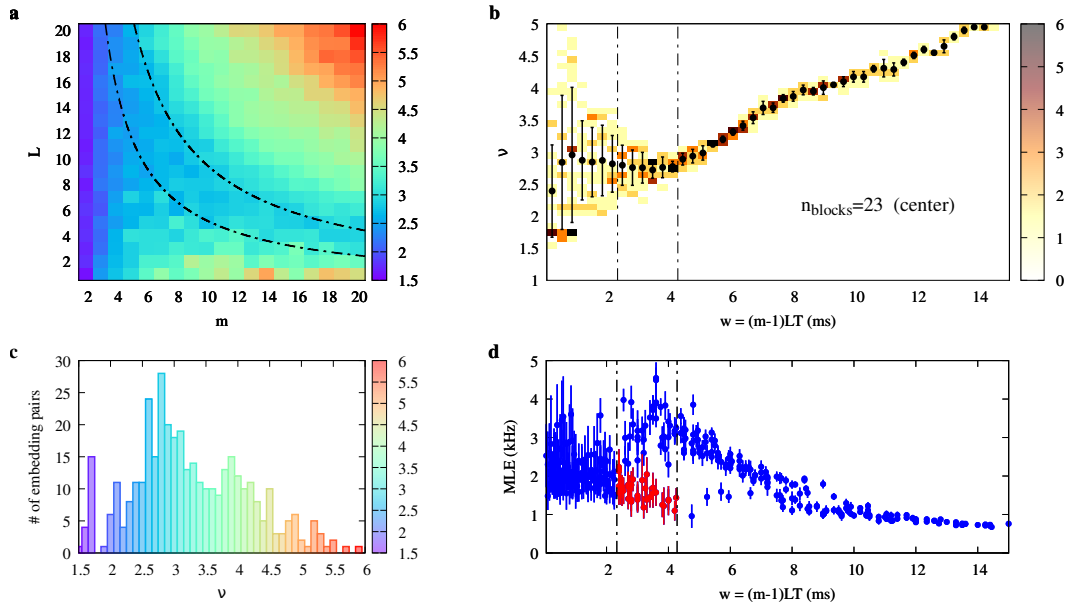


Figure 3.33: “Chasing chaos” analysis of the experimental W_{12} time series obtained by setting $V_d = 0.05$ V with 23 coupled blocks. (a) Map of estimated correlation dimension ν vs. embedding pair (m, L) . The black, dash-dotted hyperbolae bound the region of uniform ν corresponding to the interval of the embedding window w highlighted in (b) and (d). (b) Sample joint distribution of (w, ν) for the ν -map in (a). Black dots and the related errobars correspond to the expected value and the related uncertainty of ν for each given value (bin) of w . A uniformity region, highlighted by the dash-dotted vertical lines, is identified. (c) Histogram of the estimated ν . (d) Distribution of MLE as a function of w . Each point and the related uncertainty corresponds to the value assessed on an embedding pair by using the divergence rate method. A cluster of points, marked in red, can be identified in the uniformity region of (b), also highlighted here.

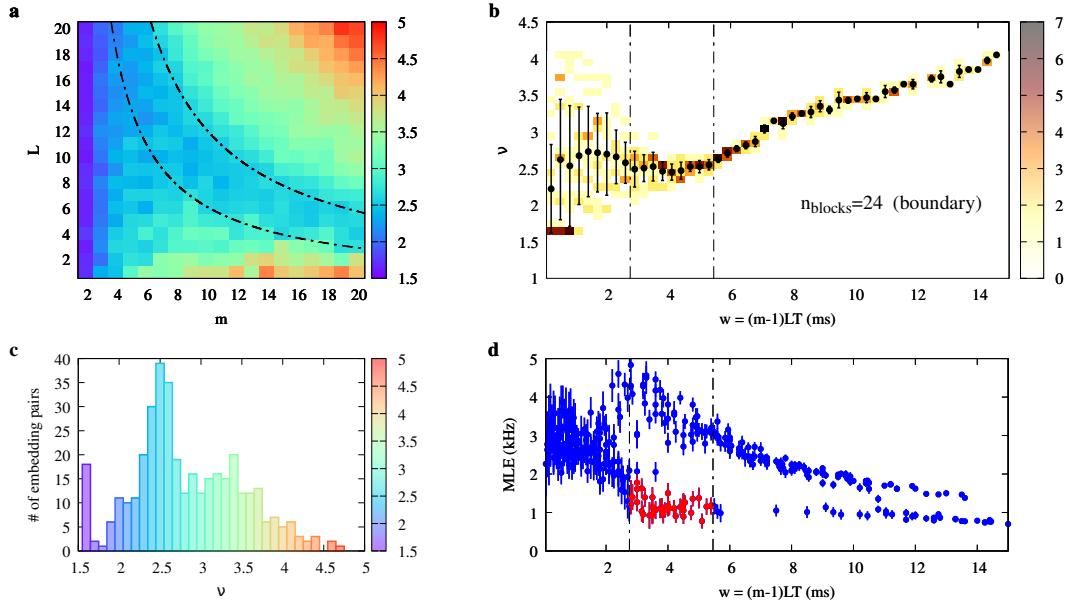


Figure 3.34: “Chasing chaos” analysis of the experimental W_1 time series obtained by setting $V_d = 0.05$ V with 24 coupled blocks. (a) Map of estimated correlation dimension ν vs. embedding pair (m, L) . The black, dash-dotted hyperbolae bound the region of uniform ν corresponding to the interval of the embedding window w highlighted in (b) and (d). (b) Sample joint distribution of (w, ν) for the ν -map in (a). Black dots and the related errorbars correspond to the expected value and the related uncertainty of ν for each given value (bin) of w . A uniformity region, highlighted by the dash-dotted vertical lines, is identified. (c) Histogram of the estimated ν . (d) Distribution of MLE as a function of w . Each point and the related uncertainty corresponds to the value assessed on an embedding pair by using the divergence rate method. A cluster of points, marked in red, can be identified in the uniformity region of (b), also highlighted here.

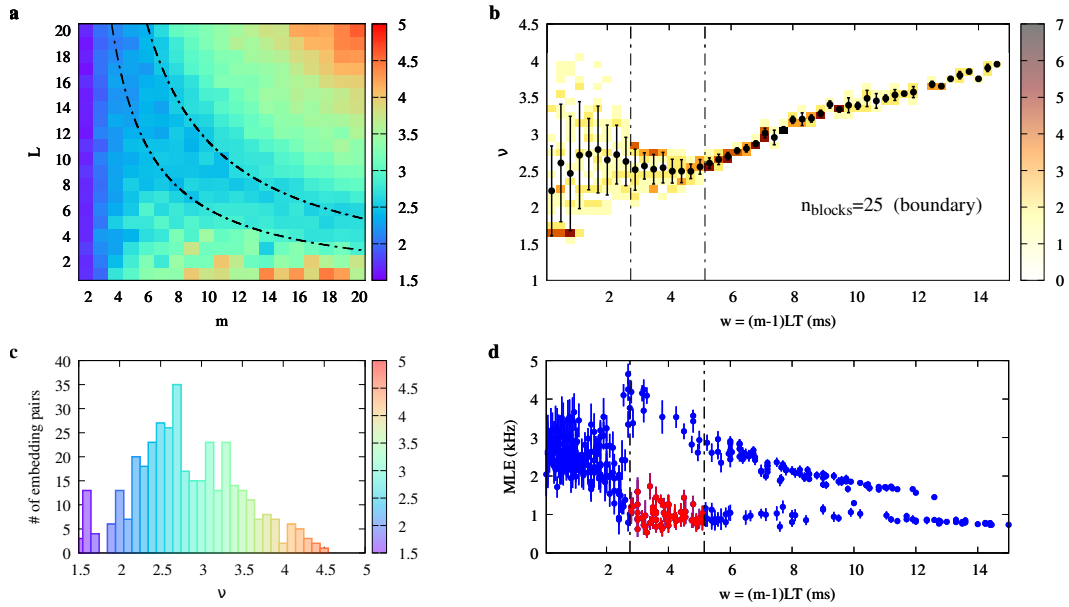


Figure 3.35: “Chasing chaos” analysis of the experimental W_1 time series obtained by setting $V_d = 0.05$ V with 25 coupled blocks. (a) Map of estimated correlation dimension ν vs. embedding pair (m, L) . The black, dash-dotted hyperbolae bound the region of uniform ν corresponding to the interval of the embedding window w highlighted in (b) and (d). (b) Sample joint distribution of (w, ν) for the ν -map in (a). Black dots and the related errorbars correspond to the expected value and the related uncertainty of ν for each given value (bin) of w . A uniformity region, highlighted by the dash-dotted vertical lines, is identified. (c) Histogram of the estimated ν . (d) Distribution of MLE as a function of w . Each point and the related uncertainty corresponds to the value assessed on an embedding pair by using the divergence rate method. A cluster of points, marked in red, can be identified in the uniformity region of (b), also highlighted here.

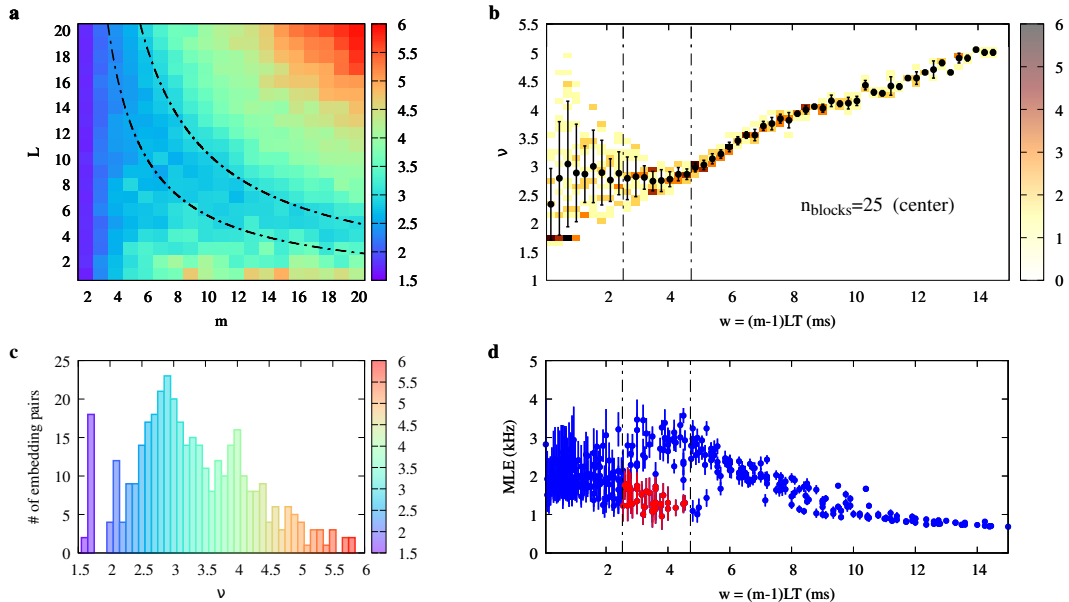


Figure 3.36: “Chasing chaos” analysis of the experimental W_{13} time series obtained by setting $V_d = 0.05$ V with 25 coupled blocks. (a) Map of estimated correlation dimension ν vs. embedding pair (m, L) . The black, dash-dotted hyperbolae bound the region of uniform ν corresponding to the interval of the embedding window w highlighted in (b) and (d). (b) Sample joint distribution of (w, ν) for the ν -map in (a). Black dots and the related errorbars correspond to the expected value and the related uncertainty of ν for each given value (bin) of w . A uniformity region, highlighted by the dash-dotted vertical lines, is identified. (c) Histogram of the estimated ν . (d) Distribution of MLE as a function of w . Each point and the related uncertainty corresponds to the value assessed on an embedding pair by using the divergence rate method. A cluster of points, marked in red, can be identified in the uniformity region of (b), also highlighted here.

3.2 Conclusions

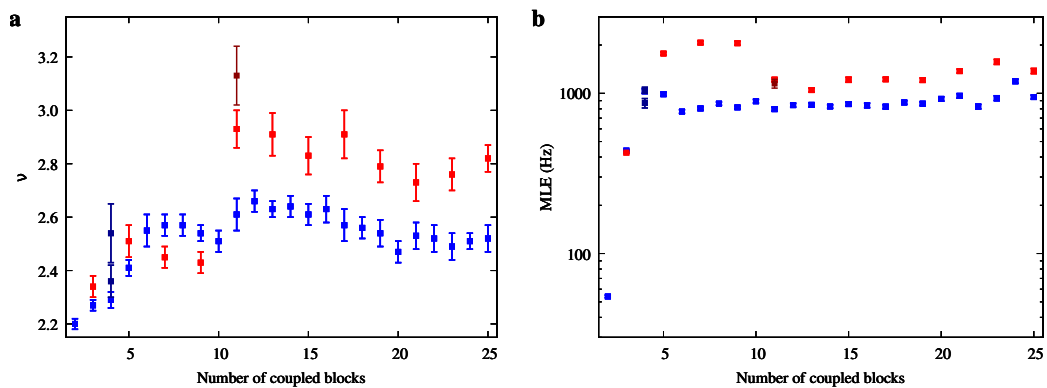


Figure 3.37: Boundary (blue) and center (red).

3.3 Attractor plots

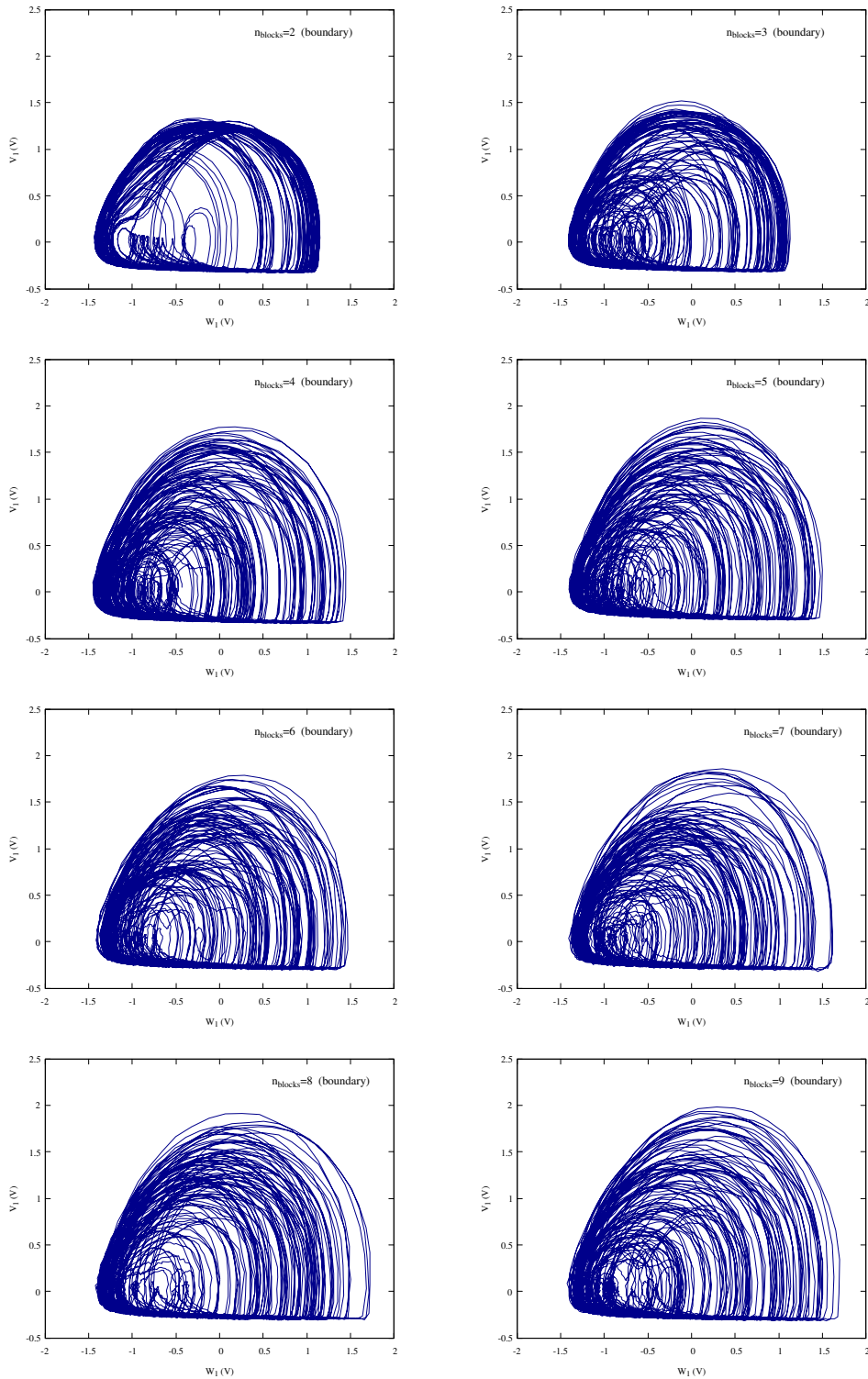


Figure 3.38: Attractors (boundary).

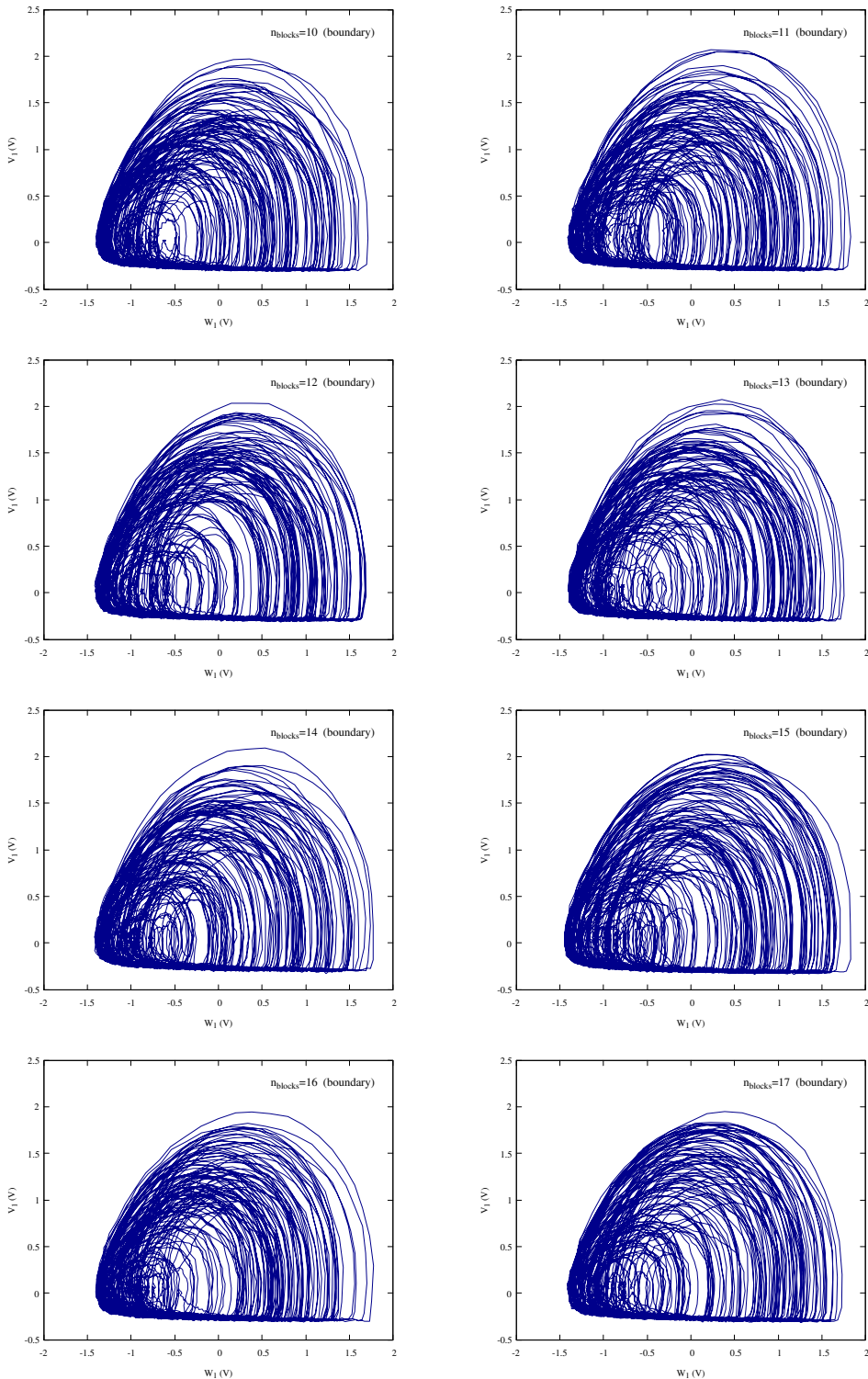


Figure 3.39: Attractors (boundary).

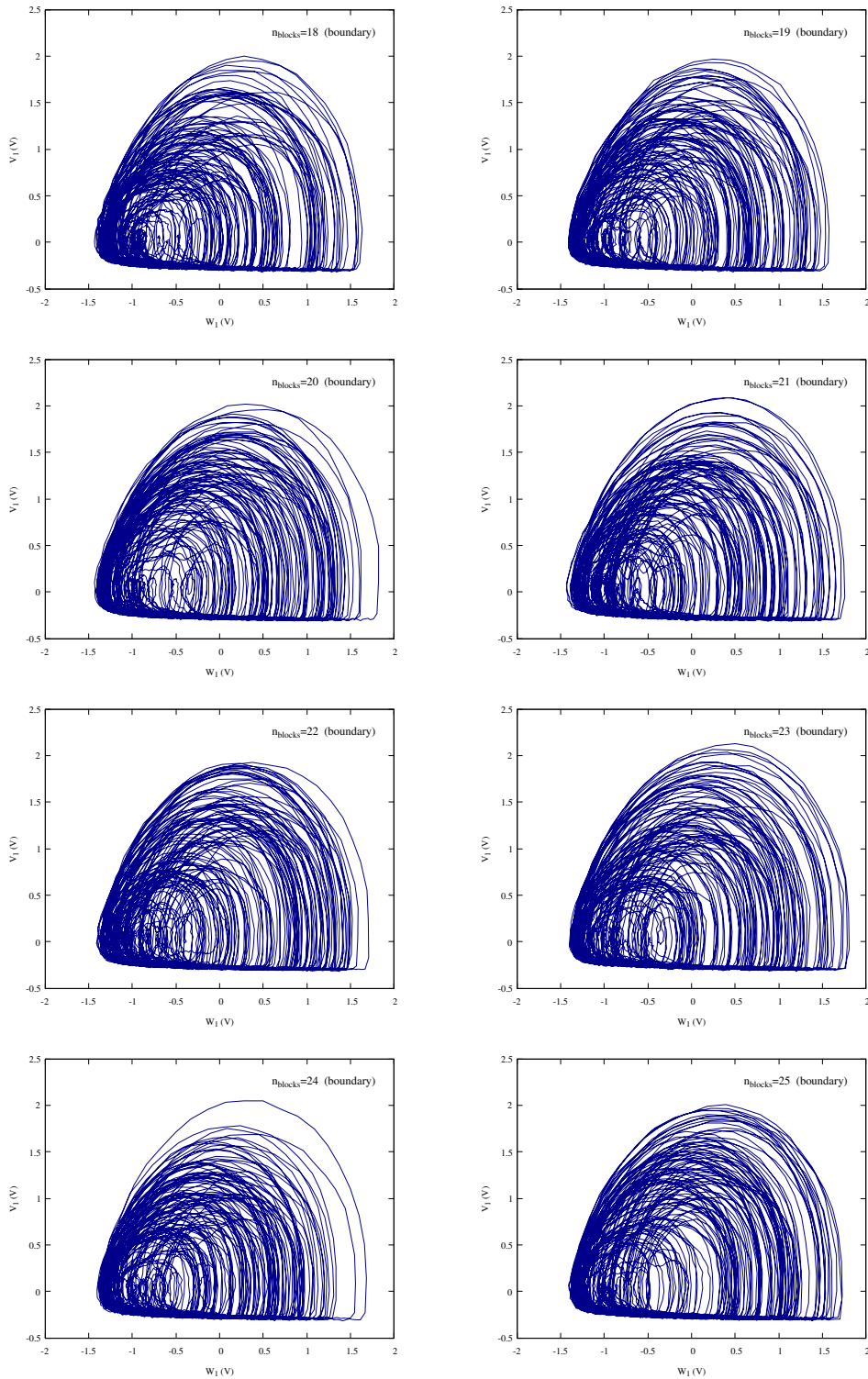


Figure 3.40: Attractors (boundary).

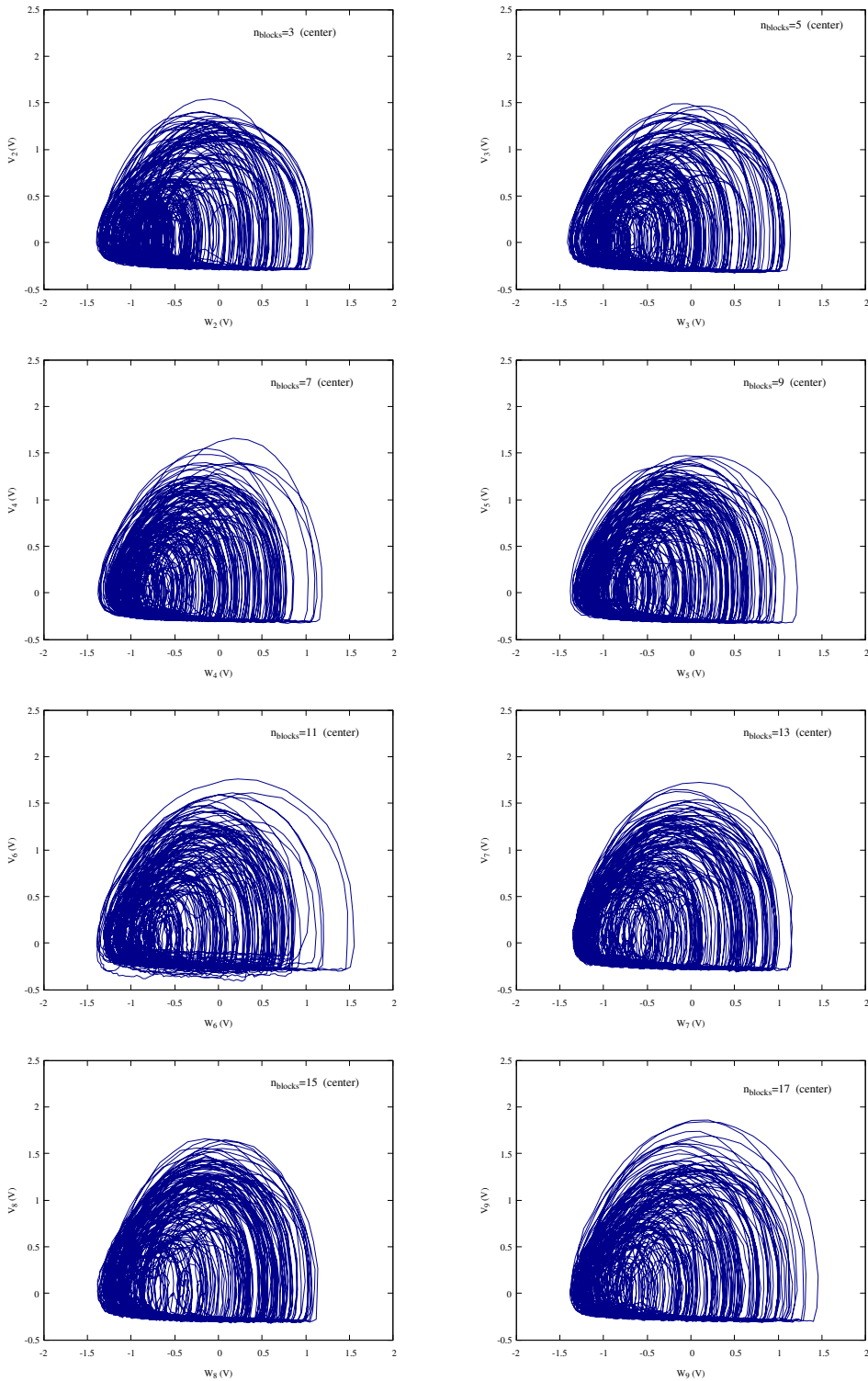


Figure 3.41: Attractors (center).

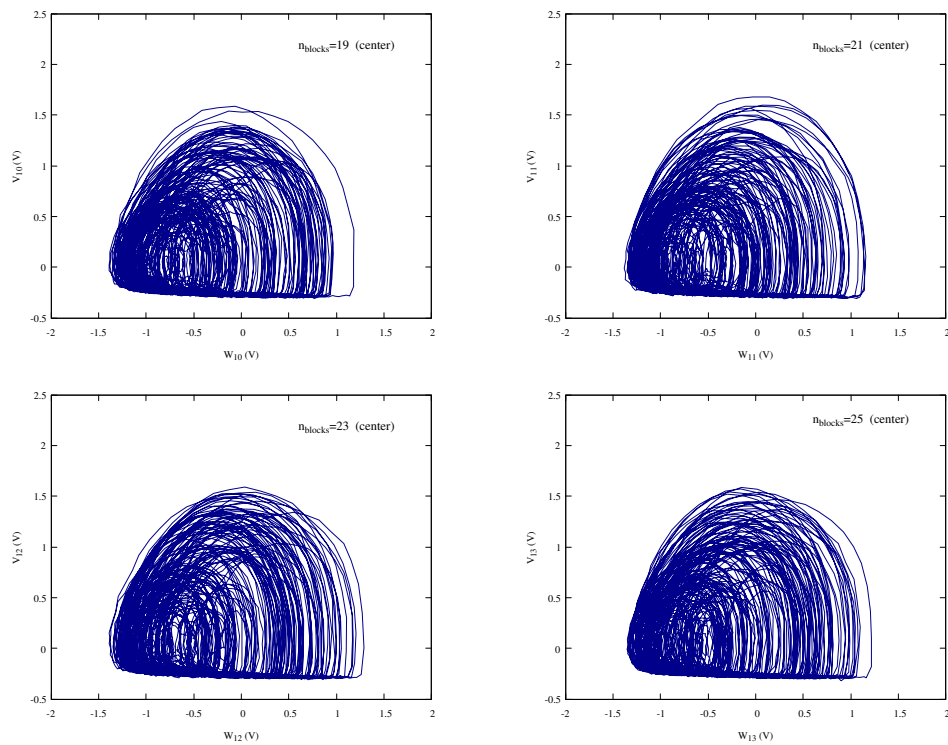


Figure 3.42: Attractors (center).

Bibliography

- [1] R. Burridge and L. Knopoff. “Model and theoretical seismicity”. In: *Bulletin of the Seismological Society of America* (1967).
- [2] Zeev Olami, Hans Jacob S. Feder, and Kim Christensen. “Self-organized criticality in a continuous, nonconservative cellular automaton modeling earthquakes”. In: *Phys. Rev. Lett.* *68*, 1244 (1992).
- [3] A. Perinelli, R. Iuppa, and L. Ricci. “A scalable electronic analog of the Burridge–Knopoff model of earthquake faults”. In: *Chaos* *33*, 093103 (2023).
- [4] S. Field, N. Venturi, and F. Nori. “Marginal Stability and Chaos in Coupled Faults Modeled by Nonlinear Circuits”. In: *Phys. Rev. Lett.* *74* (1995).
- [5] K. Popp and P. Stelter. “Stick-slip vibrations and chaos”. In: *Philos. Trans. Roy. Soc. A* (1990).
- [6] J. Theiler. “Estimating fractal dimension”. In: *Journal of the Optical Society of America A Vol. 7, Issue 6, pp. 1055-1073* (1990).
- [7] R. Devaney. *An Introduction to Chaotic Dynamical Systems*. 3rd ed. CRC Press, 2022.
- [8] E. Ott. *Chaos In Dynamical Systems*. 2nd ed. Cambridge University Press, 2002.
- [9] B. Mandelbrot. “Is nature fractal?” In: *Science*, Vol. 279, No. 5352 (1998).
- [10] C. Grebogi et al. “Strange attractors that are not chaotic”. In: *Physica 13D* 261-268 (1984).
- [11] H. Abarbanel et al. “The analysis of observed chaotic data in physical systems”. In: *Rev. Mod. Phys.*, Vol. 65, No. 4 (1993).
- [12] Ivar Bendixson. “Sur les courbes définies par des équations différentielles”. In: *Acta Mathematica* 24 (1901).
- [13] Norman H. Packard et al. “Geometry from a time series”. In: *Physical review letters* 45.9 (1980), p. 712.
- [14] Elizabeth Bradley and Holger Kantz. “Nonlinear time-series analysis revisited”. In: *Chaos: An Interdisciplinary Journal of Nonlinear Science* 25.9 (2015).
- [15] Floris Takens. “Detecting strange attractors in turbulence”. In: *Dynamical Systems and Turbulence, Warwick 1980: proceedings of a symposium held at the University of Warwick 1979/80*. Springer. 2006, pp. 366–381.

- [16] Ricardo Mañé. “On the dimension of the compact invariant sets of certain non-linear maps”. In: *Dynamical Systems and Turbulence, Warwick 1980: Proceedings of a Symposium Held at the University of Warwick 1979/80*. Springer. 2006, pp. 230–242.
- [17] Mingzhou Ding et al. “Estimating correlation dimension from a chaotic time series: when does plateau onset occur?” In: *Physica D: Nonlinear Phenomena* 69.3-4 (1993), pp. 404–424.
- [18] Peter Grassberger, Thomas Schreiber, and Carsten Schaffrath. “Nonlinear time sequence analysis”. In: *International Journal of Bifurcation and Chaos* 1.03 (1991), pp. 521–547.
- [19] Alessio Perinelli and Leonardo Ricci. “Identification of suitable embedding dimensions and lags for time series generated by chaotic, finite-dimensional systems”. In: *Physical Review E* 98.5 (2018), p. 052226.
- [20] Alessio Perinelli and Leonardo Ricci. “Chasing chaos by improved identification of suitable embedding dimensions and lags”. In: *Chaos: An Interdisciplinary Journal of Nonlinear Science* 30.12 (2020).
- [21] Martin Casdagli et al. “State space reconstruction in the presence of noise”. In: *Physica D: Nonlinear Phenomena* 51.1-3 (1991), pp. 52–98.
- [22] H.S. Greenside et al. “Impracticality of a box-counting algorithm for calculating the dimensionality of strange attractors”. In: *Physical Review A* 25.6 (1982), p. 3453.
- [23] Peter Grassberger and Itamar Procaccia. “Measuring the strangeness of strange attractors”. In: *Physica D: nonlinear phenomena* 9.1-2 (1983), pp. 189–208.
- [24] James Theiler. “Spurious dimension from correlation algorithms applied to limited time-series data”. In: *Physical review A* 34.3 (1986), p. 2427.
- [25] A Ro Osborne and A Provenzale. “Finite correlation dimension for stochastic systems with power-law spectra”. In: *Physica D: Nonlinear Phenomena* 35.3 (1989), pp. 357–381.
- [26] Alfonso M Albano, PE Rapp, and A Passamante. “Kolmogorov-Smirnov test distinguishes attractors with similar dimensions”. In: *Physical Review E* 52.1 (1995), p. 196.
- [27] Jianbo Gao and Zhemin Zheng. “Local exponential divergence plot and optimal embedding of a chaotic time series”. In: *Physics Letters A* 181.2 (1993), pp. 153–158.
- [28] Matteo Franchi and Leonardo Ricci. “Statistical properties of the maximum Lyapunov exponent calculated via the divergence rate method”. In: *Physical Review E* 90.6 (2014), p. 062920.
- [29] Leonardo Ricci, Alessio Perinelli, and Matteo Franchi. “Asymptotic behavior of the time-dependent divergence exponent”. In: *Physical Review E* 101.4 (2020), p. 042211.